MEASUREMENT OF THE PROTON FLUX AND VARIABILITY IN LOW
EARTH ORBIT WITH THE ALPHA MAGNETIC SPECTROMETER

A THESIS SUBMITTED TO
THE GRADUATE SCHOOL OF NATURAL AND APPLIED SCIENCES
OF
MIDDLE EAST TECHNICAL UNIVERSITY

BY

ÇAĞLAR KONAK

IN PARTIAL FULFILLMENT OF THE REQUIREMENTS
FOR
THE DEGREE OF MASTER OF SCIENCE
IN
PHYSICS

JANUARY 2019

Approval of the thesis:

MEASUREMENT OF THE PROTON FLUX AND VARIABILITY IN LOW EARTH ORBIT WITH THE ALPHA MAGNETIC SPECTROMETER

submitted by **ÇAĞLAR KONAK** in partial fulfillment of the requirements for the degree of **Master of Science in Physics Department, Middle East Technical University** by,

Prof. Dr. Halil Kalıpçılar
Dean, Graduate School of **Natural and Applied Sciences**   ―――――――――

Prof. Dr. Altuğ Özpineci
Head of Department, **Physics**   ―――――――――

Prof. Dr. Melahat Bilge Demirköz
Supervisor, **Physics Department, METU**   ―――――――――

Examining Committee Members:

Prof. Dr. Altuğ Özpineci
Physics Department, METU   ―――――――――

Prof. Dr. Melahat Bilge Demirköz
Physics Department, METU   ―――――――――

Prof. Dr. İsmail Turan
Physics Department, METU   ―――――――――

Prof. Dr. Ali Ulvi Yılmazer
Physics Engineering Department, Ankara Uni.   ―――――――――

Assist. Prof. Dr. Emre Yüce
Physics Department, METU   ―――――――――

Date:

I hereby declare that all information in this document has been obtained and presented in accordance with academic rules and ethical conduct. I also declare that, as required by these rules and conduct, I have fully cited and referenced all material and results that are not original to this work.

Name, Surname: Çağlar Konak

Signature   :

ABSTRACT

MEASUREMENT OF THE PROTON FLUX AND VARIABILITY IN LOW EARTH ORBIT WITH THE ALPHA MAGNETIC SPECTROMETER

Konak, Çağlar

M.S., Department of Physics

Supervisor: Prof. Dr. Melahat Bilge Demirköz

January 2019, 82 pages

AMS-02 is a general purpose high energy particle detector, installed on the International Space Station on 19 May 2011 to detect dark matter and primordial anti-matter as well as measure the cosmic particles with unprecedented statistics. AMS-02 has a unique design including a powerful magnet, large acceptance with prolonged exposure time. Protons are the most abundant charged particles among other cosmic rays above $\sim$ a few 100s MeV. An understanding of precise behaviour of them accounts for the origin, acceleration and propagation of cosmic rays. The work presented in this thesis consists of two parts, measurement of proton flux and its variability in low Earth orbit. In the first part, the proton flux analysis based on 5 years of data recorded by the AMS-02 was performed with a geomagnetic cutoff in order to eliminate the trapped flux. The second part of manuscript is about the variability of the proton flux in low Earth orbit specifically the alterations during the solar maximum in April 2014.

Keywords: AMS-02, Cosmic Rays, Low Earth Orbit, Solar Modulation

ÖZ

ALFA MANYETİK SPEKTROMETRESİ İLE DÜŞÜK DÜNYA YÖRÜNGESİNDE PROTON AKISI ÖLÇÜMÜ VE DEĞİŞİMİ

Konak, Çağlar

Yüksek Lisans, Fizik Bölümü

Tez Yöneticisi: Prof. Dr. Melahat Bilge Demirköz

Ocak 2019 , 82 sayfa

AMS-02, Uluslararası Uzay İstasyonu'nun üstünde karanlık madde ve ilkel anti-madde keşfini ve kozmik ışınların daha önce görülmemiş bir istatistikle ölçümünü amaçlayan genel maksatlı bir yüksek enerji parçacık dedektörüdür. AMS-02 güçlü mıknatısı ve yüksek kabul edilebilirliğinin içerildiği, uzatılmış maruz kalma süresiyle benzersiz bir dizayna sahiptir. $\sim$ Birkaç 100s MeV üzeri protonlar, diğer kozmik ışınlar arasında en fazla bulunan parçacıklardır. Bu parçacıkların kesin davranışları kozmik ışınların kökeni, ivmesi ve yayılmasına açıklık getirir. Bu tezdeki çalışma düşük Dünya yörüngesinde proton akısı ölçümü ve bu akının değişimini içeren 2 bölümden oluşmaktadır. İlk bölümde, yazı 5 yıllık AMS verisi ile gerçekleştirilmiş proton akısı analizine odaklanacaktır. İkinci bölüm ise, bu akının zamanla değişimleri ile ilgilidir ve 2014 solar maksimum zamanındaki değişimler detaylandırılacaktır.

Anahtar Kelimeler: AMS-02, Kozmik Işınlar, Düşük Dünya Yörüngesi, Solar Modülasyon

Along the Journey to the Big Picture

ACKNOWLEDGMENTS

TABLE OF CONTENTS

LIST OF FIGURES

FIGURES

LIST OF ABBREVIATIONS

AMS	Alpha Magnetic Spectrometer
ISS	International Space Station
CR	Cosmic Rays
TRD	Transition Radiation Detector
TOF	Time of Flight
RICH	Ring Imaging Cherenkov
ECAL	Electromagnetic Calorimeter
POCC	Payload Operating Control Centre
eV	Electron Volt
GeV	Giga Electron Volt
GV	Giga Volt
TV	Tera Volt
SEP	Solar Energetic Particles
ISM	Inter Stellar Medium
GZK	Greisen-Zatsepin-Kuz'min
SAA	South Atlantic Anomaly
CME	Coronal Mass Ejection
TR	Transition Radiation
TTCS	Tracker Thermal Cooling System
ACC	Anti Coincidence Counter
SPS	Super Proton Synchrotron
TDRS	Tracking and Data Relay Satellite
PMT	Photo Multiplier Tube
SPENVIS	Space Environment Information System

CHAPTER 1

INTRODUCTION

Protons are the most abundant charged particles among cosmic rays above a few $\sim$100s MeV. Understanding the origin, acceleration and propagation of protons is important to discern the precise behaviour of cosmic rays [16]. An accurate measurement of proton spectrum in low Earth orbit can be provided by the Alpha Magnetic Spectrometer (AMS-02). Taking advantage of the AMS-02 as a unique spectrometer, solar modulation of protons can also be investigated onboard the International Space Station (ISS), shown in Figure 1.1.

AMS-02 is a multi-purpose high energy particle physics detector which was flown to the ISS with the Space Shuttle Endeavour on the 16th of May, 2011 and has been operating on the ISS since the 19th of May, 2011. The detector can measure cosmic rays in the GeV to TeV energy range with unprecedented accuracy and statistics.

The main objective of AMS-02 is the precise measurement of the Cosmic Rays (CR) composition which could reveal a signature for dark matter and presence of primordial anti-matter. Moreover, the large acceptance and a high rate of data acquisition can enable time dependency analysis of the flux.

The key elements included in the spectrometer are a Tracker, a Transition Radiation Detector (TRD), a Time of Flight (ToF) system, a Ring Imaging CHerenkov (RICH) Detector, an Electromagnetic CALorimeter (ECAL) and a permanent magnet. The full reconstruction of particle can be performed using particle properties such as charge, velocity, momentum or energy provided by the subdetectors.

1
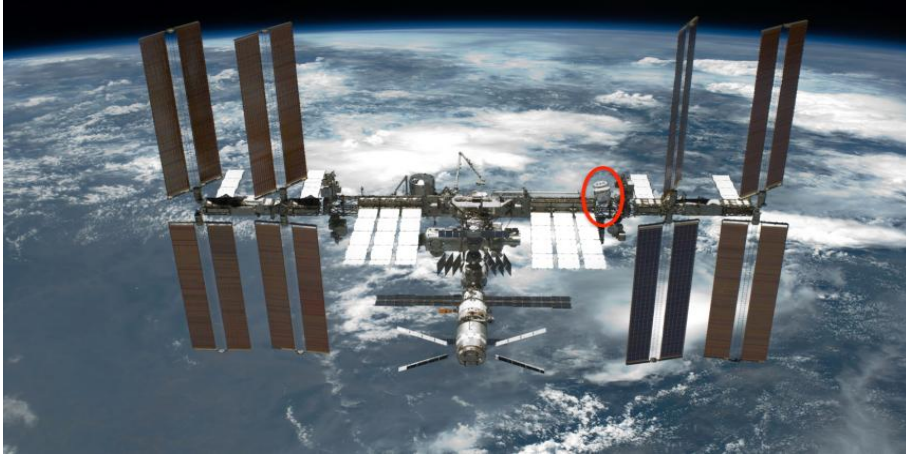
Figure 1.1: Alpha Magnetic Spectrometer indicated with a red circle on the International Space Station in low Earth orbit [1].

With 7 years of data in orbit, several results have been published. Important results are as followers:

• Electron and positron flux have different behaviour at ~ 30 GeV in their magnitude and energy dependence. Both measurements show no fine structure or observable anisotropy [17, 18, 19, 20].

• In general cosmic ray flux decreases with 2.7 order of rigidity which is particle momentum divided by its charge. Concerning this fact, both proton and helium fluxes show similar rigidity dependence [16, 21].

• Although the antiproton, proton and positron fluxes show nearly same behaviour above ~ 60 GV, electron flux is distinctly different from them [22].

• The boron to carbon flux ratio is in good agreement with the Kolmogorov theory of turbulence [23].

• The primary cosmic rays He, C and O and the secondary cosmic rays Li, Be and B show identical rigidity dependence in different rigidity ranges [24, 25].

• For the first time the charge-sign dependent modulation was analyzed for leptons during solar maximum. There is a smooth transition in positron to electron flux ratio

after solar magnetic field reverses [26].

• The spectral index for nitrogen flux shows identical behaviour with primary He, C and O cosmic rays above ~ 700 GV [27].

• Longterm time evolution of protons follows an 11-year solar cycle where number of sunspots reach maximum and minimum caused by a 22-year cycle of Sun's magnetic field polarity[28]. Modulations caused by solar activities have been observed at Low Earth Orbit. The last solar maximum was in April 2014.

In this thesis, the solar modulation of the proton flux for 5 years of data taking will be presented based on 560 million events. In chapter 2, cosmic rays origin, their acceleration and propagation will be discussed. Chapter 3 will focus on AMS-02, instrumentation, operations at Payload Control Centre (POCC) and data transfer from the ISS. Identification of protons and the proton flux measurement with systematics will be presented in chapter 4. In addition, the precise measurements of proton flux in the kinetic energy range from 1 to 100 GeV will be compared with the results of the space environment information system, SPENVIS. In chapter 5, variability of the proton flux in time and in different rigidity ranges will be presented and finally, the thesis will be concluded.

CHAPTER 2

COSMIC RAY PHENOMENOLOGY

Cosmic Rays (CRs), discovered by Victor Hess in 1912 [29], are high energy particles spanning many orders of magnitude in energy. They travel almost at the speed of light and reach the Earth's upper atmosphere from all directions. Apart from sub-atomic particles, they are composed of nuclei, ranging from the lightest to the heaviest elements in the periodic table.

The cosmic radiation is dominated by protons and helium nuclei above a few $\sim 100s$ MeV outside of Earth's atmosphere. In other words, of cosmic rays about 99 percent are protons and helium nuclei. The remaining part, on the other hand, is constituted by electrons, heavier nuclei and a very small fraction of antimatter particles such as positrons and antiprotons. Among those particles, protons, electrons, helium, carbon, oxygen and some other nuclei accelerated at astrophysical sources are called primaries. Other particles such as lithium, beryllium and boron not synthesized in stars, but produced in interactions between primaries and interstellar gas are called secondaries [7].

The number of particles per unit of energy, area, solid angle and time (measured in GeV^{-1} m^{-2} sr^{-1} s^{-1}) also known as the flux is analyzed and presented here. In fact, the total cosmic ray flux corresponds to thousands of particles per square meter per second at low energies (E $\sim 10^9$ eV) and less than one particle per square kilometer per century at the highest energies (E $\sim 10^{20}$ eV) [30]. The power-law energy distribution of the energy spectra of cosmic rays shows an energy dependence,

$$\frac{dN(E)}{dE} \sim E^{\gamma} \tag{2.1}$$

where N denotes the number of cosmic rays at the top of the atmosphere and γ is a spectral index which is related with shock speed in acceleration mechanism of cosmic rays, detailed in acceleration section.
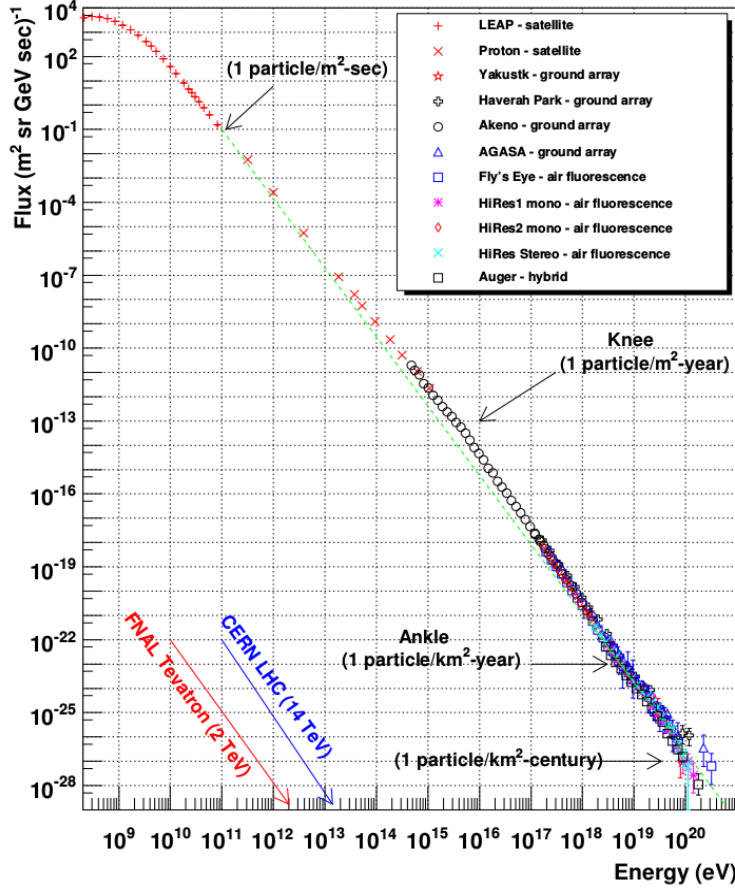
Figure 2.1: The energy spectrum of cosmic rays from satellite, ground array and air fluorescense experiments are shown compared with the energy reach of recent accelerators. A knee at 10^6 GeV and an ankle structure at 10^9 GeV are observed [2].

Two remarkable features observed in the spectra are so-called a "knee" structure and an "ankle" structure shown in Figure 2.1. The figure shows the first break of the spectra known as the knee at 10^{15} eV [31]. In addition, the spectral index of cosmic rays changes from 2.7 to 3.0 at this point. However, because of the low abundance of cosmic rays above 10^{18} eV, there is not much known for the second break, the ankle, where the spectral index returns back to 2.7. It might be the result of a contribution

6

coming from extragalactic sources [32]. At the higher end of this plot (Figure 2.1), the statistics are very low. The interaction of cosmic rays and photons from the Cosmic Microwave Background result in a theoretical cutoff beyond which cosmic spectrum is suppressed. The cutoff at the energy $\sim 10^{20}$ eV is called Greisen-Zatsepin-Kuz'min (GZK) cutoff. This energy approximately corresponds to a change in the observed CR flux [33].

At the low energy end of this plot ($< 10^9$ eV), the flux as a function of kinetic energy changes with phases of the Sun, which is called the solar modulation effect. The modulation effect is related to an 11-year solar cycle caused by a magnetic field polarity which will be discussed in the last section, heliosphere and magnetosphere. During the solar cycle, number of sunspots reach a maximum and later a minimum. As a result, winds and coronal mass ejections representing a large amount of energy are formed. While solar activity increases, the disturbance it causes in the interplanetary magnetic field increases as well [2]. The Earth's geomagnetic environment can be represented as a cavity existing in the solar wind. In order to quantify the external magnetic field influence on charged particles, a quantity named as rigidity is defined as momentum divided by per elementary charge (Ze), given as number of electrons [34],

$$R = \frac{p}{Ze} \tag{2.2}$$

The multiplication of the magnetic field strength and a measurement of the radius of the circular motion of a charged particle in the presence of a uniform magnetic field also gives the rigidity, which is $R = B.r = B/\rho$, where ρ is a curvature of the charged particle's path and r is particle's radius of gyration in a uniform magnetic field. The greater the rigidity, the smaller the deflection of a charged particle in the external magnetic field.

This part of the thesis gave fundamental information of cosmic rays, composition and energy spectra, as well as geomagnetic interaction. In the following sections CRs origin, acceleration and propagation are detailed respectively. In addition, the last section will provide more information about heliosphere and the Earth's geomagnetic environment especially to understand low energy cosmic ray behaviour.

2.1 Cosmic Ray Origin

Possible sources for cosmic rays are supernovae, active galactic nuclei, pulsars, gamma-ray bursts and the Sun. Cosmic rays are categorized as solar, galactic and extragalactic cosmic rays according to their respective sources. There is no clear explanation for energy level of the transition from the galactic to the extra-galactic cosmic rays. The ankle structure might be a feature for the transition [35].

Solar cosmic rays, ranging in energy between $\sim 10^7$ eV and $\sim 10^{10}$ eV, are ejected primarily in two ways, solar winds and coronal mass ejections which are solar activities released in energy by the Sun. They are also called solar energetic particles (SEPs). Detecting SEPs is important because they provide information about non-thermal processes in the plasma between the Sun and the Earth and also the SEP acceleration, whether it is a flare or a shock related to a coronal mass ejection. During the 11-year solar cycle, SEPs affect the Earth's magnetosphere and even its atmosphere in several ways. The behaviour of SEPs depends on not only their energies but also their altitude and latitude in the atmosphere. Sudden changes in the rigidity cutoff, Forbush decreases, solar X-ray bursts and energetic electron showering, which will be detailed at the end of chapter, carry information on the effects of SEP on the atmosphere. This influence always has been taken into account due to its importance of radiation conditions in near Earth orbit especially for spacecraft systems [36].

Having energies below 10^{15} GeV (below knee), CRs are originated by galactic sources such as supernovae, their products and pulsars. Supernova remnants can also be accepted as a main source of galactic cosmic rays [37].

Very high energy CRs, which are not easily measurable because of low statistics, consist of heavy nuclei up to Iron. It is known that they do not originate from supernova remnants. A hypernovae which is an extremely energetic supernova could be the source of these extragalactic cosmic rays [38]. Nevertheless interactions of cosmic rays and photons through Cosmic Microwave Radiation should be used to comprehensively examine signals coming from hypernovae to confirm whether they could be the origin of extragalactic CRs.

Interstellar Medium (ISM) is the matter and radiation including gas in ionic, atomic,

and molecular form, as well as dust and cosmic rays. Two physics processes, acceleration and propagation, shape the spectra of CRs in the ISM [39]. The next sections will explain both processes in detail.

2.2 Cosmic Ray Acceleration

As stated above supernova remnants are thought to be the main source of cosmic rays and the main objective of this section is to explain the acceleration of CRs by these remnants.

Enrico Fermi proposed two cosmic ray acceleration mechanisms. The first proposal [40] is related to the interaction between a moving magnetized gas cloud and charged particles. These particles gain energy in head-on collisions with magnetic mirrors which is a magnetic field configuration in which a charged particle is reflected from a high density magnetic field to low density magnetic field. However they lose energy in head-tail collisions. With each collision, the particle gains energy proportional to $(v/c)^2$. This is why the process is called second-order Fermi acceleration. The acceleration at the end of the process is slow and not sufficient to explain the cosmic ray energy spectrum.

The most promising mechanism for explaining the spectrum of galactic cosmic rays is the acceleration near strong shock-fronts caused by supernova explosions. Strong shocks are irregularities propagating through the ISM with a velocity much greater than the speed of sound in that medium. This acceleration mechanism [41] was proposed by Enrico Fermi to give a comprehensive explanation of cosmic rays spectrum and it is called first-order Fermi acceleration. In this mechanism, since the particle gains energy proportional to (v/c), the mechanism derives its name as first order Fermi acceleration. The media in front of the shock and behind it differ in density. CRs gain kinetic energy from the gas behind the shock and disturb the isotropic environment in front of the shock. As long as CRs are scattered backwards again, the acceleration is repeated multiple times. This process continues until the energy losses balance the acceleration rate and the resulting energy spectrum follows a power law

with roughly constant spectral index [3],

$$\frac{dN(E)}{dE} \sim E^{-p} \qquad (2.3)$$

where p, the spectrum index, is ~ 2.1, compared with the observed value of 2.7. The spectrum index shows shock speed relation based on acceleration mechanism for cosmic ray flux.

In conclusion, the first-order Fermi acceleration mechanism provides more efficient way for cosmic rays acceleration than second-order Fermi acceleration mechanism.

2.3 Cosmic Ray Propagation

Cosmic rays propagation that they undergo along the way is important in order to explain the acceleration models. It explains how cosmic rays propagate in the Interstellar Medium. Spallation reactions on the ISM are the key physics process to account for production of secondaries from primaries. Parameters such as magnetic field structure, interaction cross sections, CR source type and density, the size of the galaxy are related parameters to explain the cosmic ray propagation along the way. While the intergalactic magnetic field strength is a few μG [42], the interstellar magnetic field is observed as 10 μG [43] with small uncertainty in the Galactic center region. There are a few models explaining cosmic rays propagation in the Galaxy. The diffusion model provides information for cosmic ray transport below about 10^{17} eV. On the other hand, the leaky box model can describe the cosmic ray propagation in terms of confinement volume and border conditions before CRs escape from galactic region.

2.3.1 The Diffusion Model

The diffusion model is the most adequate propagation model to describe the transport of cosmic rays together with a convection in the Galaxy [44] since it uses the propagation in the Inter Stellar Medium (ISM). The ISM is predominantly composed

of hydrogen, as well as significant amounts of helium and very small quantities of carbon, oxygen and nitrogen. The diffusion model can make comprehensive understanding to propagation of cosmic rays in ISM [45] with diffusive process. Diffusive process, in fact, determines the propagation by accounting for interaction between particles and irregularities in the galactic magnetic field. The diffusion model can also explain composition and isotropy of cosmic rays.

2.3.2 The Leaky Box Model

The Leaky Box model is, on the other hand, a common model for describing confinement in the galaxy. In other words, it assumes that sources are uniformly distributed in a confined volume where CR escape time is independent of position. This steady-state approach models cosmic ray density by using CR production and loss balanced in time. Unlike diffusion model, there is no spatial dependence in the approximation of this model. There are two assumptions to account for propagation of cosmic ray in the leaky box model. The first one is ignoring energy loss in the ISM and the second one is a kinetic energy preservation during spallation reactions.The various nuclides appearing in cosmic ray fluxes and spallation reactions actually show that this model is a complex system including many equations. Fortunately, many approaches can be used to simplify these equations, detailed in [46].

To sum up, two different propagation models show importance of the ISM in propagation process. Diffusion model uses the ISM for environment and variables to account for CR propagation by using diffusive process. On the other hand, the Leaky Box model uses any confined volume where sources are uniformly distributed independent of position. And it ignores energy loss in the ISM.

2.4 Heliosphere and Magnetosphere

The solar wind, which is dominant in the bubble-like region surrounding the Sun, determines the boundaries of the heliosphere. This tenuous magnetized plasma escaping from the Sun is a mixture of ions and electrons that fills the space between the Sun and the Earth. Solar winds lose their dominance in the borders of the helio-

sphere, so-called heliopause where the outward pressure of the solar wind balances the pressure of the incoming ISM, about 123 astronomical units from the Sun[47].

The Earth's magnetic field, tilted by 10 degrees relative to its rotation axis, is approximately a magnetic dipole that creates a cavity in the solar wind in the vicinity of the Earth, so-called magnetosphere. The magnetosphere, shown in Figure 2.2, has surrounding features called the magnetopause, bow shock and magnetosheath, which are formed by the interaction between the solar wind and the Earth's magnetic field. It reaches down to the upper atmosphere where the ionized part of the atmosphere is located. Since the solar wind is not static, the magnitude and shape of the magnetosphere change in time [48]. When the solar wind first encounters the heliopsheric field, a bow shock occurs. The magnetosphere ends where the magnetized plasma pressure and solar wind pressure balance each other. This is called the magnetopause. The magnetosheath represents a region between the bow shock and the magnetopause in which density of the charged particles is much lower than beyond the bow shock.

In the magnetosphere, charged particles are trapped in closed orbits known as Van Allen radiation belts, drifting around the Earth and confined by the intrinsic magnetic field.

The combined effects of magnetic fields of the Earth and the Sun, as well as the solar wind, form the complex electromagnetic configurations that affect the propagation of cosmic radiation entering the heliosphere and the magnetosphere. The terrestrial magnetic field places a geomagnetic cutoff that depends on the geomagnetic latitude in the vicinity of the Earth. Rigidity cutoff quantifies the ability of a particle to penetrate the magnetic field at a precise location.
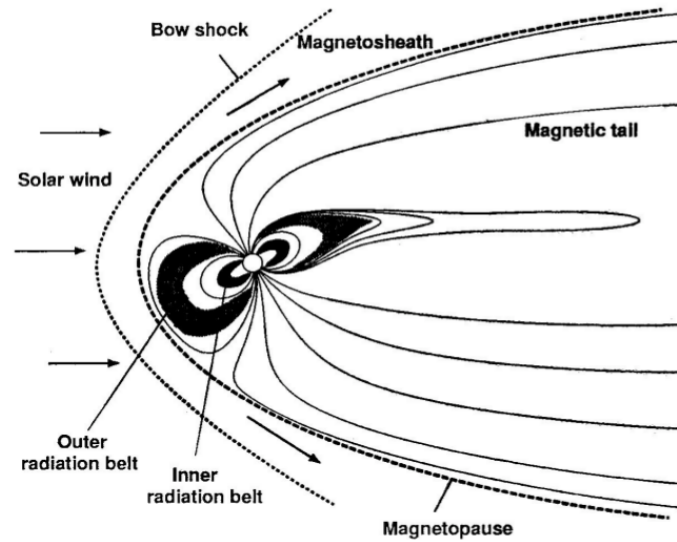
Figure 2.2: The magnetosphere of the Earth. It has surrounding features called the magnetopause, bow shock and magnetosheath, which are formed by the interaction between the solar wind and the Earth's magnetic field. A bow shock occurs when the solar wind encounters heliopsheric field. The magnetopause is located where the magnetized plasma pressure and solar wind pressure balance each other. The magnetosheath represents a region between the bow shock and the magnetopause in which density of the charged particles is much lower than beyond the bow shock [3].
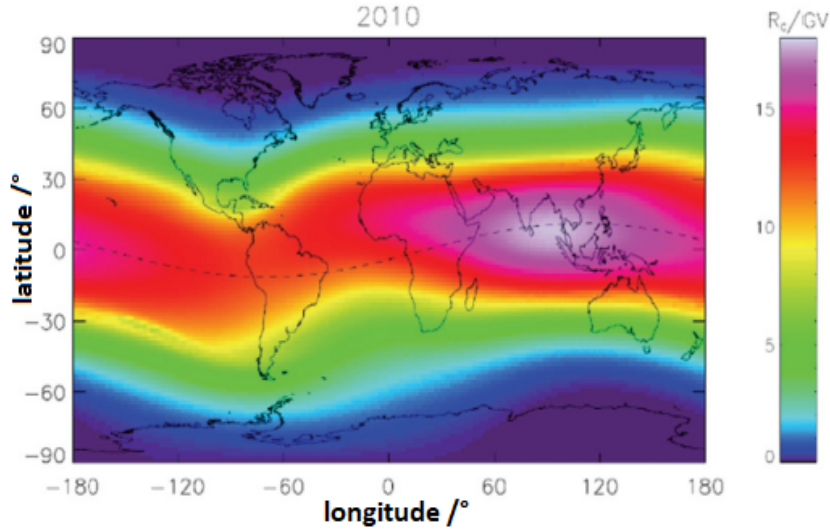
Figure 2.3: The rigidity cutoff in terms of latitude and longitude. The cutoff takes its maximum values around the equator and decreases towards the polar regions [4]

.

In other words, it is the minimum momentum per charge ($R_c = p/Ze$) also equals to the magnetic field strength multiplied by the Larmor radius ($R_c = r_L B$). In the presence of a uniform magnetic field, charged particles can make a circular motion. The radius of the circle is called Larmor radius or gyroradius. In the calculation of rigidity cutoff, the International Geomagnetic Reference Field (IGRF) is used as a spherical harmonic model with parameters obtained from satellites and ground-based experiments [49]. The rigidity cut-off, shown in Figure 2.3 which varies from equator to poles, causes charged particles to have different rigidity as a function of latitude and longitude. For the incident charged particle coming from space, since its momentum and magnetic field lines are perpendicular to each other on equator, these particles bend towards to the poles. At poles, particle momentum direction and magnetic field lines are parallel to each other. Therefore these particles have no magnetic field effect and can penetrate Earth's atmosphere.

The Figure 2.4 shows the intensity of the geomagnetic field in a standard global model IGRF 2000. Furthermore the white part of the figure represents the South Atlantic Anomaly (SAA) where the magnetic field intensity is below 32000 nT. Because of the

14

small magnetic field intensity, rigidity cutoff is also low in this region. Therefore most of charged particles which have rigidity higher than the rigidity cutoff at SAA, can pass to the Earth's atmosphere. The SAA is a large-scale characteristic that deviates from an ideal magnetic dipole field and has a comparatively low strength field in the region encompassed by the South Atlantic, some parts of South America, South Africa and Antarctica. The main source of the SAA is located in the outer core of the Earth, where an opposite magnetic flux induces a decrease in the magnetic field at the SAA latitudes. No clear long-term correlations between SAA and the Earth's magnetic field have been observed so far [5].
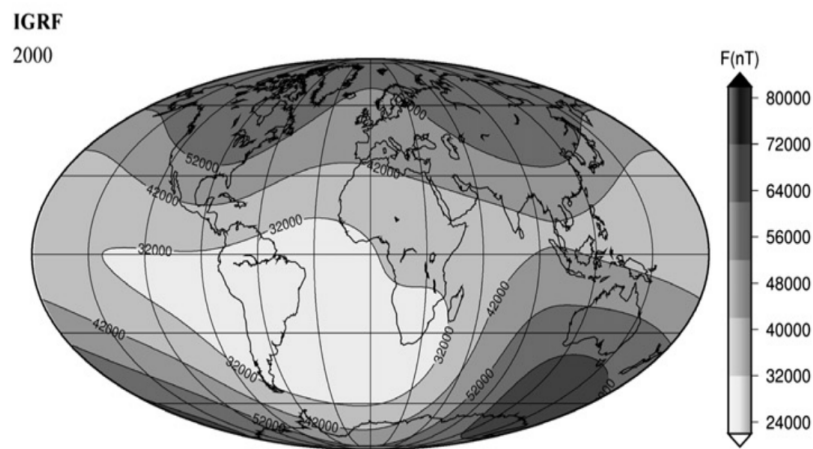
Figure 2.4: The intensity of the geomagnetic field in a standard global model IGRF 2000. The white part represents magnetic field intensity below 32000 nT, known as the South Atlantic Anomaly (SAA) [5].

Cosmic ray intensity is correlated with solar activities and modulated throughout the Earth's orbit. Solar activities are a result of an 11-year solar cycle caused by the Sun's magnetic field polarity flip [50]. The magnetic field of the Sun is thought to be formed by the movement of plasma over the surface of the Sun. Unlike the Earth's dipole magnetic field, the Sun has much more complex and tangled structure with many magnetic poles. This large magnetic structure flips every 11 years. While this intricate structure flips, the developing unit abilities cause many sunspots observed on the surface of the Sun, each of which has a magnetic field strength 1000 times greater than the Earth's maximum magnetic field. The number of sunspots oscillates

15
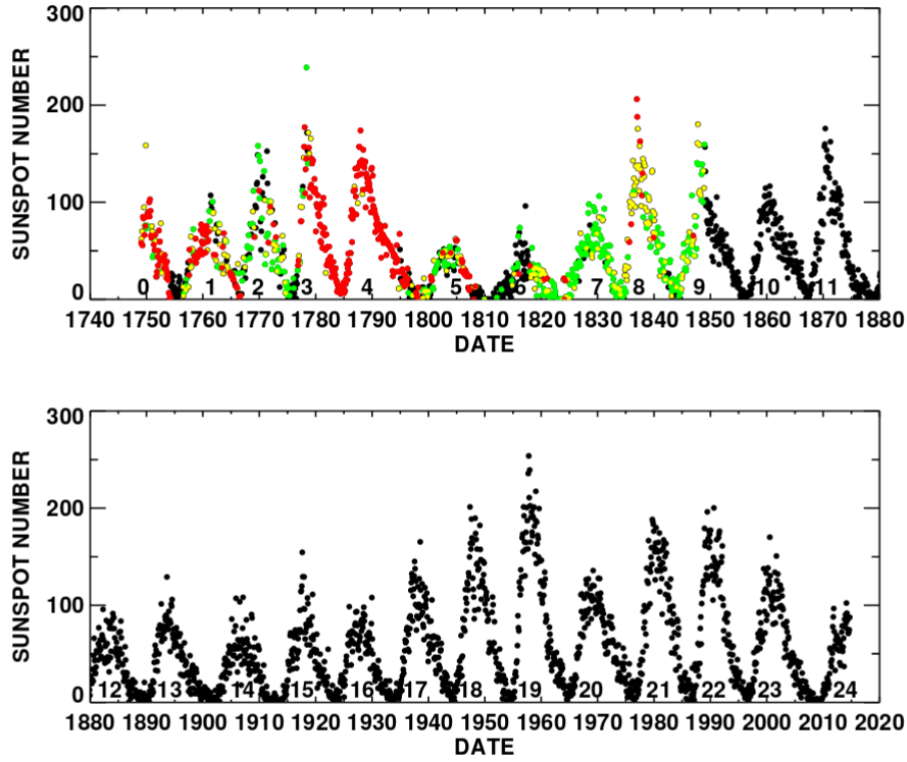
Figure 2.5: Monthly averages of the daily Sunspot Numbers since year 1750. Each black point gives the average sunspot number for a month of observation using daily data. Reliable solar observations have been performed since 1818 and before that date, some days are missing from the record. Observations for months with 1-10 days of missing data are shown in green while 11-20 days of missing data are shown in yellow. Observations for months with 20 days of missing data are shown in red. An estimation was used to complete missing days for the time period.

between the solar maximum and minimum. In other words, sunspot numbers reach maximum and minimum in these periods. Figure 2.5 shows monthly averages of the daily Sunspot Numbers since 1750. Each black point gives the average sunspot number for a month of observation using daily data. Reliable solar observations have been performed since 1818 and before that date, some days are missing from the record. Observations for months with 1-10 days of missing data are shown in green while 11-20 days of missing data are shown in yellow. Observations for months with 20 days of missing data are shown in red. An estimation was used to complete missing days for the time periods [51].

16

Beginning from the sunspot minimum, solar cycle takes about 11 years and the solar maximum is recorded almost halfway. The sunspots form and disappear without inducing long-lasting changes in the Sun's magnetic structure. Consequently, a large amount of energy is released in the form of solar winds and coronal mass ejections [52]. Solar winds and Coronal Mass Ejections (CME) are recorded as electromagnetic radiation ranging from radio waves to gamma rays. The largest CME hit to the Earth is known as the Carrington event in 1859; it allowed researchers to make observations about the relationship between solar activity and Earth's geomagnetic field. In 1989, a CME event lead to a knock-out of transformers and 6 million people remained without electricity for half a day. The Great Halloween Storms, a series of solar flares and coronal mass ejections, observed in 2003 caused power outages and electronic problems for many satellites [53].

Solar and magnetospheric activities are generally observed in time scales ranging from hours to 27 days. For instance, 27 days time duration characterizes recurrent solar activities, so-called Bartels rotations days [54]. Bartels rotation is a counting system similar to the Carrington rotation. For Carrington rotations, sun spots and solar eruptions are observed in the same relative frame every 27.2753 days. Carrington rotation takes Earth's rotation around the Sun into account where as the Bartels rotation does not. Bartels rotation is another counting system which is equal to 27 days for a fixed feature on the Sun to rotate to the same apparent position as viewed from Earth. Because of this reason there is 0.2753 days time difference between two rotation systems. Daily and hourly observations are also performed to understand magnetic storms and magnetic substorms. Particle acceleration events or plasma irregularities can be analyzed in minutes and seconds.

In conclusion, effects of the Sun to the heliosphere and magnetosphere, are detailed by explaining 11 year solar cycle and magnetic field polarity flip. In chapter 5, these effects will be analyzed with 5 year data recorded by the AMS-02 in low Earth orbit.

2.4.1 Forbush Decreases

In many cases the solar cosmic ray intensity suddenly decreases up to 20 percent following a coronal mass ejection (CME) or solar flare. This is associated with geo-
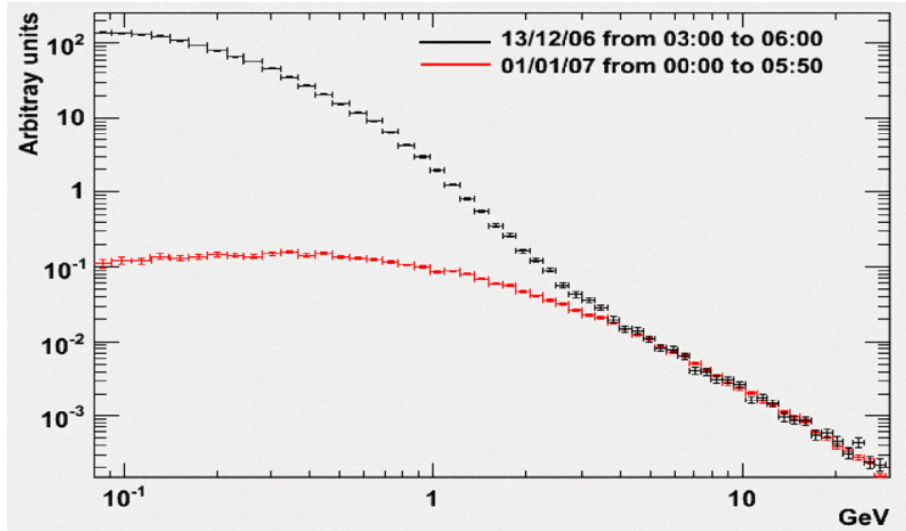
Figure 2.6: Relative count rate observed during Forbush decrease of January 2005 with data recorded by Jungfraujoch IGY neutron monitor.

magnetic storms and is known as the Forbush decreases. The minimum is maintained for a few hours, but the recovery to back normal levels may take days or even weeks. There are three factors which characterize the magnitude of a Forbush decrease;

• Size of the CME

• Magnetic field strength of the CME

• Closeness of the CME to the Earth [55]

Both solar activities eject large amounts of material from the Sun as detailed in previous section. When the material including a large magnetic disturbance reaches to the Earth, galactic cosmic rays are swept away in the vicinity of the Earth. This process has been measured up to a few 10 GeV energy because of magnetic field strength of the solar wind plasma [55].

An example is shown in Figure 2.6. Relative count rate was observed during Forbush decrease of 21 January 2005 with data recorded by Jungfraujoch IGY neutron monitor [56]. Neutron monitor can measure charged particles predominantly protons and helium nuclei so that it can record 11-year sunspot cycle and 22-year magnetic cycle effects on atmosphere.

18

2.4.2 Solar Energetic Particles

Solar energetic particles are very high-energy particles emitted by the Sun. They consist of protons, electrons and alpha particles with kinetic energies ranging from keV to GeV [57]. Their sources are the above-mentioned solar flares and coronal mass ejections.
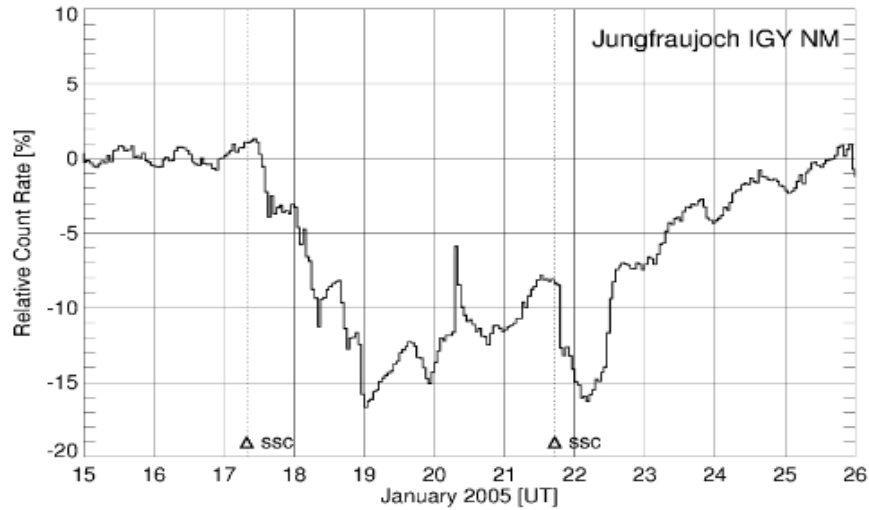
Figure 2.7: Proton energy spectrum for a 3 hour long big solar event on December 13, 2006. The proton flux is suppressed shown in black during 3 hour long solar event and have a quite solar period shown in red [6].

Figure 2.7 shows comparison of proton energy spectrum for a 3 hour long big solar event on December 13, 2006. The proton flux is suppressed shown in black during 3 hour long solar event and have a quite solar period shown in red. The reason for change in spectrum at that time was a coronal mass ejection.

2.4.3 Neutrinos

Neutrinos are one of the most debatable particles especially for last century. From their discovery to mass measurements it has been almost 100 years that scientists have focused on them to account for their behaviours to understand Standard Model

19

which assumed that neutrinos were zero-mass particles.

Solar neutrinos are so important to probe dynamics of the Sun including nuclear fusion process which originate the solar neutrinos in the heliosphere. It all starts from pp chain reaction where hydrogen nuclei (protons) end up as α particles (helium-4 nuclei) at the Sun.

One of the experiment which measures the emitted solar neutrinos is located in the Homestake mine in South Dakota. The emitted neutrinos, weakly interacting particles, were counted using a huge tank of chlorine. The reason for deep underground experiment is to have solar neutrinos eliminated from background including cosmic rays. However the accumulated neutrino composition showed mismatch from predicted one, known as solar neutrino problem [58].

Solar neutrinos are key particles which need flavor change to explain relation between predicted and experimental accumulated neutrinos so called neutrino oscillations. After set of measurements, it has been proved that neutrinos have masses much smaller than other known elementary particles [59].

Since neutrino oscillations are sensitive only to the difference in the squares of the masses, it has not proven yet neutrino mass scale. Cosmology states that at there is a fixed ratio between the number of neutrinos and the number of photons in the cosmic microwave background. All these unknown situations require more comprehensive explanations to understand the mechanism behind neutrino mass scale and physics beyond SM.

To sum up, fundamental features, origin, propagation and acceleration of cosmic rays are the subjects of the chapter. Moreover, heliospheric environment and magnetosphere were detailed in the concept of 11-year solar cycle of the Sun. The important energy releases that are formed by the Sun are known as solar activities. Not only they carry solar energetic particles but also change magnetosphere and have huge effect in the low energy cosmic rays flux. The analysis performed in the thesis will especially focus to this spectrum of the proton flux. 5 year data will show time variation of proton flux up to 10 GV in detail. Next chapter will give information for the AMS-02 detector including instrumental parts, reconstructions, data acquisition and

monitoring. The AMS-02 is a multipurpose magnetic spectrometer which is sensitive to measure charged particles and photons with time precision up to 150 ps and 10 μm tracking resolution.

CHAPTER 3

ALPHA MAGNETIC SPECTROMETER

AMS-02 is a general purpose magnetic spectrometer to perform precise measurements of cosmic ray fluxes above the Earth's atmosphere. It will be operating on board the International Space Station during its lifetime, which is expected to be extended to 2024. Already in its 7 years of operation, AMS-02 has collected more than 120 billion events.

The identification of cosmic rays is performed in a redundant way with contribution from different subdetectors. The subdetectors, detailed in following sections, use different kinds of physics processes to identify and measure particles.

The first section of chapter will give detailed information about AMS-02's sub-detectors and reconstruction methods. In the second section, the data acquisition and monitoring of the AMS-02 will be discussed.

3.1 The AMS-02 Detector

AMS-02, shown in Figure 3.1, is a high acceptance particle detector on the International Space Station. The coordinate system of the AMS is concentric with the center of the permanent magnet supplying 0.15 T magnetic field. While the z-axis of the AMS points vertically upwards, the x-axis is aligned with the main component of the magnetic field. An identification of particle properties is made by using data from several subdetectors: A Transition Radiation Detector (TRD), a Tracker, a Time of Flight (TOF) system, a Ring Imaging CHerenkov detector (RICH) and an Electromagnetic CALorimeter (ECAL). In addition to those subdetectors, there is an

Anti Coincedence Counters (ACC) around the permanent magnet to avoid misreconstructed events. The following sections describe each subdetector and the magnet as well as reconstruction of particles in detail.
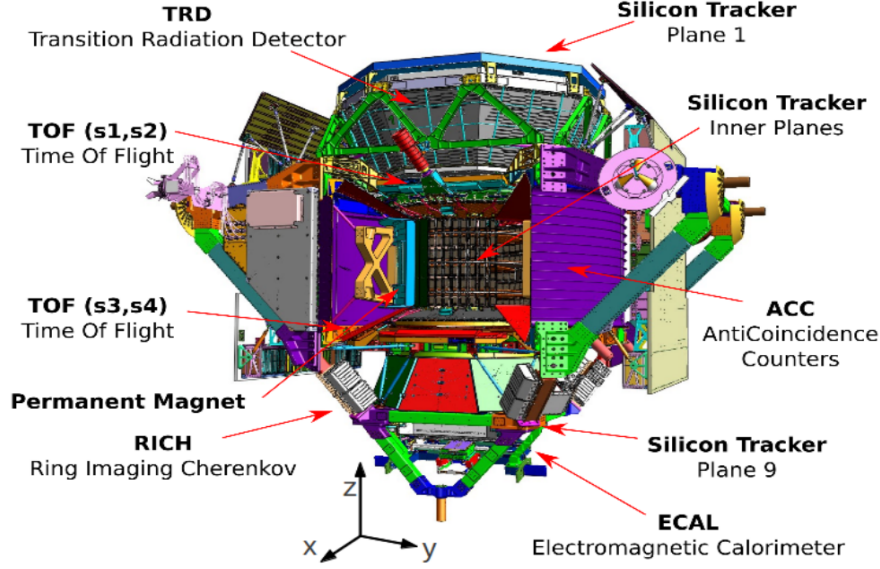
Figure 3.1: A drawing of the Alpha Magnetic Spectrometer, each subdetector is labelled. Concentric coordinate system with permanent magnet is shown in the Figure as well. [7]. While the z-axis of the AMS points vertically upwards, the x-axis is aligned with the main component of magnetic field.

3.1.1 The Transition Radiation Detector

The Transition Radiation Detector (TRD) is designed to achieve positron (or electron) and proton separation using the γ (Lorentz) factor sensitivity of radiation emitted when a charged particle transition between two media with different dielectric constants [60]. For different particles with similar velocities and momentum, transition radiation, whose intensity depends on Lorentz factor, is used to identify particles with different masses.

Transition radiation occurs when a relativistic particle moves across the interface of two media with different dielectric constants. The intensity of it is proportional to the

24

Lorentz factor of charged particles.

Figure 3.2: The Transition Radiation Detector of the AMS-02 in the clean room [8].

The TRD in the clean room is shown in Figure 3.2. The aforementioned two media in the TRD are a TR radiator and vacuum. A particle whose Lorentz factor is greater than 1000 emits an appreciable transition radiation in the X-ray region of the spectrum (1-30 KeV) [61]. The emitted radiation in 20 mm of fleece is detected in Xe/CO_2 filled proportional wire straw tubes [60]. This fleece and straw tube structure is repeated in 20 layers to increase the probability of identification. Moreover, the TRD can be used as a 3D tracking device because of the $90°$ horizontal rotation of 12 central layers with respect to the upper and lower layers of the detector [7].

Signals from the 20 layers of proportional tubes are combined in a TRD estimator in order to differentiate between $e^{\pm}$ and protons in the TRD. The TRD estimator is created from the ratio of the log-likelihood probability of the $e^{\pm}$ hypothesis to that of the proton hypothesis [18]. After a set of measurements, the rejection power of the TRD estimator for protons measured at %90 $e^{\pm}$ efficiency is 10^3 to 10^4.

3.1.2 The Magnet and The Tracker

The AMS coordinate system is concentric with the permanent magnet, shown in Figure 3.3, which is centered in the detector. The toroid filled by the magnet has inner diameter 1.12m, outer diameter 1.30m and height 0.80 m. As a result, the geometric acceptance of the magnet is obtained as $0.82m^2$sr [62].

The strength of the permanent magnet is 0.15 T in the x-direction, with negligible dipole moment so that the magnet is preserved from the effect of torque and electronics interference on the ISS [63].
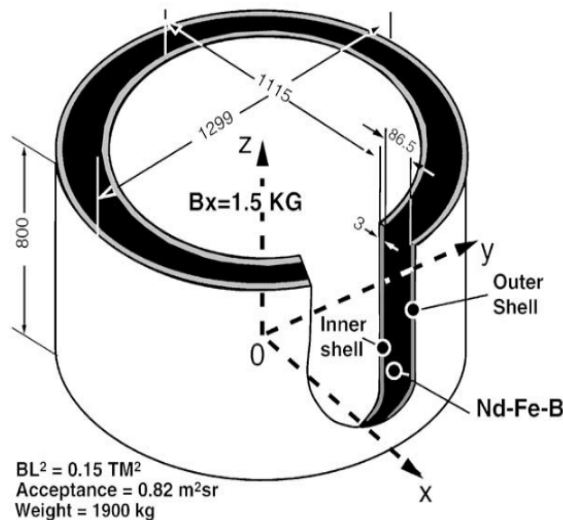
Figure 3.3: AMS-02 permanent magnet supplying a 1.5 KG dipole magnetic field. It is composed of 64 sectors of Nd-Fe-B blocks with strength aligned in the x-plane. The bending power is measured as 0.15 Tm^2 [9].

The permanent magnet of AMS-02 was also used in the AMS-01, precursor flight on the space shuttle Discovery (mission STS-91, in June 1998). A superconducting magnet was built for use in AMS-02 with helium coolant refiles with future shuttle flights. However, since shuttle flights were cancelled, it was exchanged with the AMS-01 permanent magnet [64].

26

The Tracker inside the magnet can measure the rigidity and charge with sign, shown in Figure 3.4, using the bending power of the magnet. Nine layers are included in the Tracker. The first layer is located on the very top of the detector and ninth layer is mounted between the RICH and the ECAL. The two outer layers provide information for whether the charged particle is from incoming (penetrating to the detector from first layer of the Tracker) or outgoing (penetrating to the detector from last layer of the Tracker) direction. Rest layers are surrounded by a permanent magnet supplying 0.15 T magnetic field aligned with the x-axis of the AMS coordinate system [18].

Each layer is made out of silicon microstrip sensors, which were developed to provide precise tracking with 10 μm resolution [65].
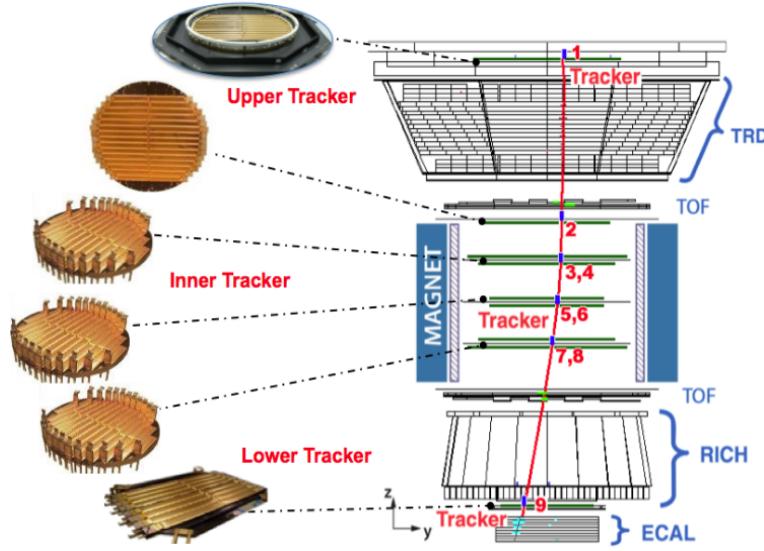
Figure 3.4: The Tracker of AMS-02. From very top of the detector to the last layer between RICH and ECAL, all silicon layers are shown aside [10].

$$\frac{dE}{dx} \propto z^2 \tag{3.1}$$

A charged particle crossing the silicon creates deposited energy which is proportional to the square of the charge of the particle [66], given in Equation 3.1. The charge resolution can be used to identify the charge of particles up to iron.

27

Heat is produced by the leakage current of the Tracker silicon sensors and this has to be removed by a cooling system to keep the noise levels low. For the Tracker of the AMS-02, this system is called the Tracker Thermal Cooling System (TTCS) [67]. The CO_2 cycle in the TTCS collects the waste heat by evaporating liquid CO_2 to gaseous state.

3.1.3 The Time of Flight Detector

The Time of Flight detector, shown in Figure 3.5 during construction, is made of two planes of scintillator paddles. Each of them consists of two layers of counters which are then placed on top and bottom of the permanent magnet. The scintillation counters are optically coupled at both ends with photo multiplier tubes (PMT) so that the time resolution is observed approximately to be 150 ps [68]. In order to measure particles velocity up to %98 of the speed of light, Upper and Lower TOF layers are located roughly 1.2 m apart in z [69].

An ionization loss of charged particle causes an ultraviolet scintillating light which is absorbed by wavelength shifting fibers. Finally, the shifted light is transported to PMTs for readout. If a particle traverses the upper and the lower Time of Flight layers, the particle is said to be inside the AMS acceptance. Data acquisition is started by a trigger signal and then all of the subdetectors are warned.
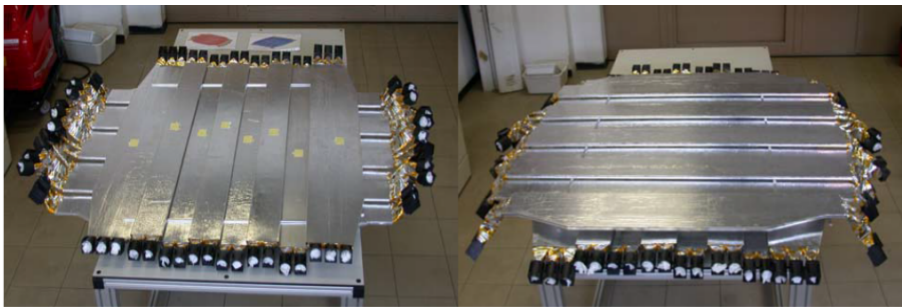
Figure 3.5: The upper and lower part of the Time of Flight detector, one of the key instruments for velocity and mass measurements. The TOF system can give information about charge of the particles up to $Z = 8$, number of protons in nuclei.

The trigger rate can reach up to 2 kHz with an average event size of about 2 KB. The trigger rate is observed to be very high in the polar regions (~ 1 kHz) and in the South Atlantic Anomaly (~ 1.4 kHz) due to geomagnetic cutoff value when compared to the equatorial region [70].

Similar to the Tracker, Time of Flight detector also can give information about the charge of the particle using energy deposition. Nevertheless, the charge measurement of ToF is only reliable up to $Z = 8$, number of protons in nuclei, since the TOF has a spatial point resolution of 7 μm [71].

3.1.4   The Anti-Coincidence Counters
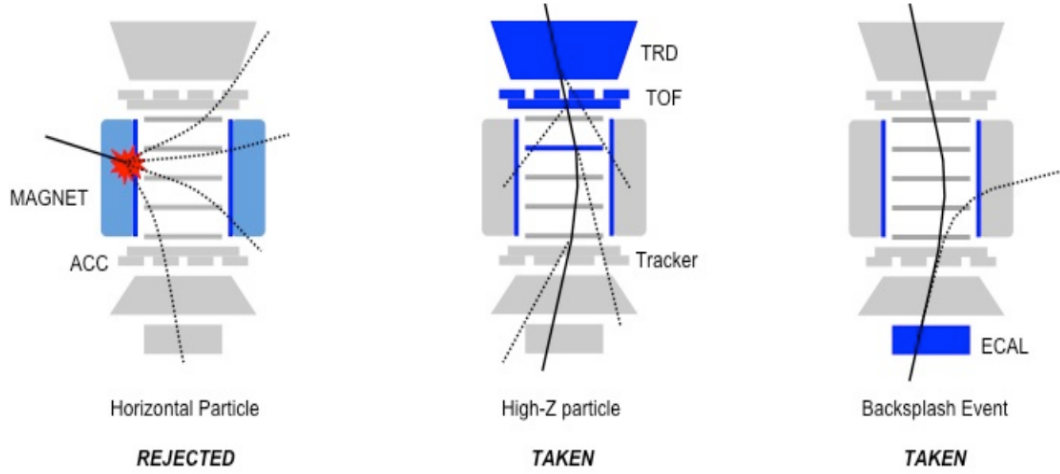
Figure 3.6: High-Z particles or backsplashed events are accepted by the detector, while particles from side of the detector are not accepted as events since these particles lead to misreconstruction of event in the Tracker [11].

The Anti Coincidence Counters (ACC) system eliminates the particles outside of the AMS-02 acceptance. For the purpose of vetoing the particles to assure clean track reconstruction, the ACC is located around the Tracker inside the inner bore of the permanent magnet. Particles from either secondary interactions coming from inside detector or from the sides are detected in the ACC. Also, the trigger veto system allows for trigger rate to be decreased during periods of high intensity flux, e.g. in the

polar regions or the South Atlantic Anomaly [72].

Similar to the Time of Flight detector, the ACC system is composed of 16 scintillation detectors with a thickness of 8 mm. The Figure 3.6 shows the working principle of the trigger logic for particles coming from different directions and hitting the ACC. While high-Z and backsplash particles are accepted by the detector as event, particles from outside of the AMS-02 acceptance are vetoed.

3.1.5 The Ring Imaging Cerenkov Counters

The Ring Imaging Cherenkov Detector (RICH) plays a major role in event reconstruction. The Figure 3.7 shows the full drawing of the assembled detector (right) including materials and a photograph of photomultiplier tube cell assembly (left). The RICH is located above the ECAL and below the lower TOF layers. The RICH provides a precise measurements of particle velocity and charge of a charged particle.
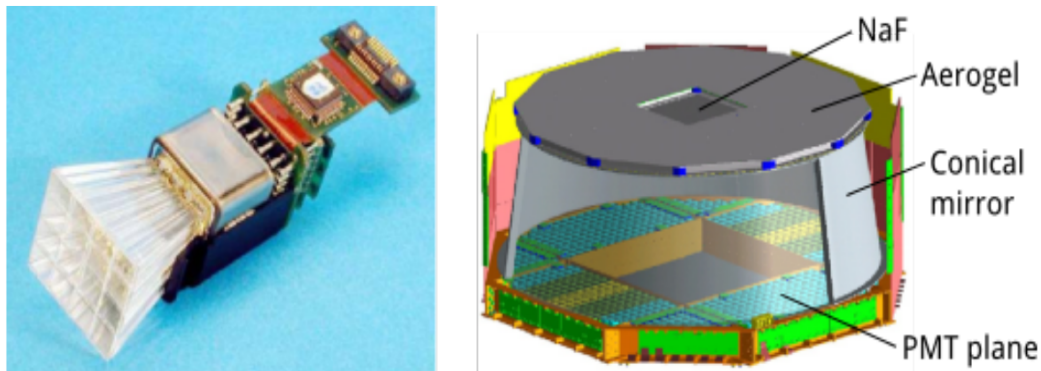
Figure 3.7: A photograph showing the photomultiplier tube cell assembly (left), the full drawing of including materials used inside (right) [12].

In the central part of radiator is made of sodium fluoride with a refractive index n of 1.33 corresponding to a Cherenkov threshold of $\beta > 0.75$ and the outer area of radiator is surrounded by the aerogel with a refractive index n of 1.05 corresponding to a Cherenkov threshold of $\beta > 0.953$. The emitted Cherenkov light is detected by the plane with 680 photomultiplier tubes [73].

RICH can help reconstruction of Lorentz beta and mass of the charged particle. Interaction of a particle with velocity greater than the speed of light in a material can cause Cherenkov light to be emitted in a cone with an opening angle θ. Relation between the Lorentz factor beta, the refractive index n and the opening angle is given in Equation 3.2 [66].

$$\theta_c = arccos(\frac{1}{n\beta}) \tag{3.2}$$

Mass reconstruction will be detailed in the reconstructions part of the chapter.

3.1.6   The Electromagnetic Calorimeter

The bottom-most detector of the AMS-02 is the Electromagnetic Calorimeter (ECAL). The energy deposition in the ECAL can help distinguish between protons and leptons. An electron can produce an electromagnetic shower dominated by bremsstrahlung and pair production inside the ECAL. The ECAL is made up of 9 superlayers, with an active area of 64.8 times 64.8 cm^2 and corresponds to 17 radiation lengths. The superlayers of ECAL can also provide 3D shower profile of an electron [74].
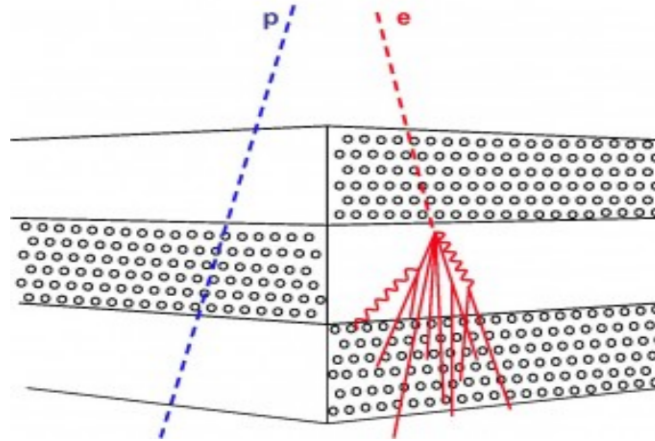
Figure 3.8: Schematic drawing of the interaction of a proton and an electron inside the ECAL. While the proton only leaves behind ionization energy loss, the electron showers electromagnetically [11].

In the example shown in Figure 3.8, interaction of a proton and an electron are given in the superlayers of the ECAL. While the electromagnetic shower on the right is caused by an electron, the proton is measured only by its ionization energy loss. Energy resolution of leptons as a function of incident particle energy is given in Equation 3.3 from proton, electron and positron beams produced in the CERN Super Proton Synchrotron (SPS) in 2010 [75].

$$\frac{\sigma(E)}{E} = \frac{(10.4 \pm 0.2)\%}{\sqrt{E}} + (1.4 \pm 0.1)\% \tag{3.3}$$

3.1.7 Reconstructions

The reconstruction of particle properties such as magnitude and sign of charge, velocity, energy, mass and momentum and hence particle identification are made in a redundant way with the aid of several subdetectors. Main equations used in reconstruction of these parameters are given in this subsection.

Important piece of information provided by the Tracker is rigidity, which is the momentum divided by charge of the particle. When a charged particle experiences the Lorentz force in the magnetic field, the curvature of their path is in the y-direction. Provided that the track of the charged particle is reconstructed from signals left in different layers of the Tracker, the curvature $\rho = \frac{1}{r}$ can be reconstructed in the detector as well. The multiplication of the magnetic field strength and a reconstruction of the Larmor radius of the charged particle gives the rigidity, which is $R = Br$. The Maximum Detectable Rigidity (MDR) is measured to be approximately 2 TV for Z=1 [76].

TOF measures the traversal time of a particle between the top and bottom layers. By using the particle flight time and trajectory length, it is possible to reconstruct the cosmic ray's beta (velocity/c). Simultaneous measurement of beta and momentum enables to identify mass of the particle [70],

$$\frac{p}{c} = m\beta\gamma \tag{3.4}$$

RICH mass reconstruction is derived using the charge and rigidity information from the Tracker. From the equality of the centripetal and the Lorentz force, the mass equation is deduced,

$$m = RZ \frac{\sqrt{1 - \beta^2}}{c\beta} \quad (3.5)$$

where R is rigidity.

Comparison of the signal from different particles with 300 GeV energy left in different subdetectors is shown in Figure 3.9. While magnetic field bends positively charged particles in one direction, negatively charged particles are oppositely bent in the other direction. There are two ways to detect gamma rays in the detector. The first one is electron positron pair conversion in the detector and the second way is the electromagnetic shower in the calorimeter without producing any signal in the detectors above. Even though proton and helium nuclei show similar signals in different subdetectors, they differ in terms of size due to different rest mass of the particles.

Figure 3.9: Signals left by a 300 GeV electron, positron, proton, anti-helium or gamma particle in different subdetectors. A photon may either convert to electron-positron pair inside the detector or shower in the calorimeter without leaving any signal in the detectors above [13].

3.2 AMS on the International Space Station

Operation and maintenance of the AMS-02 are highly dependent on the electronic supplies of ISS. While ISS solar panels provide power to its systems, the data down-link between AMS-02 and ground relies on the Tracking and Data Relay Satellite (TDRS) system in geostationary orbit. 24 hours monitoring is performed in the Pay-load Operation Control Centre at CERN in order to ensure that electrical and physical parameters of AMS-02 are inside the pre-determined healthy intervals. The following sections detail the data acquisition and monitoring of the AMS-02.

3.2.1 Data Transferring from ISS
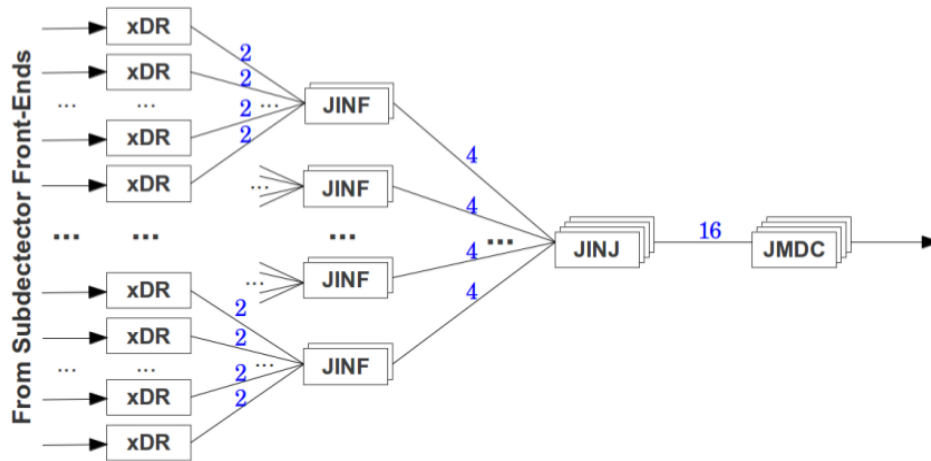
Figure 3.10: Data transfer from subdetectors to main computer, JMDC. Each xDR has information on the current event from each subdetector. Then the data are transferred to interface board JINJ, holding up to 4 events. After one more recording in the higher level interface board, the data are passed to final acquision system of the the JMDC [7].

Data taking begins with a trigger signal initiated by either the Time of Flight system or the Electromagnetic Calorimeter. The recorded signal warns subdetectors so that each subdetector sends its current measurement to the data reduction boards (xDR).

Then the data from all xDRs are collected by an interface board (JINF-x) of each subdetector. Each buffer belonging the interface board holds up 4 events in its buffer. Afterwards the data recorded with an event size of 2 kByte from all subdetector electronics are transferred to a higher level interface board (JINC) in order to reach the final data acquisition system of AMS-02: the main computer (JMDC) [77]. The JMDC checks for data loss especially during communication loss between ISS and ground. Whole process is shown in Figure 3.10.

3.2.2 AMS Payload Operation Control Centre (POCC)

The ISS orbits the Earth with an altitude changing between 370-460 km and velocity of $\sim$ 29000 km per hour, completing one tour around the earth in approximately 1.5 h. The latitude range of the ISS is between $52°$ N and $52°$ S.
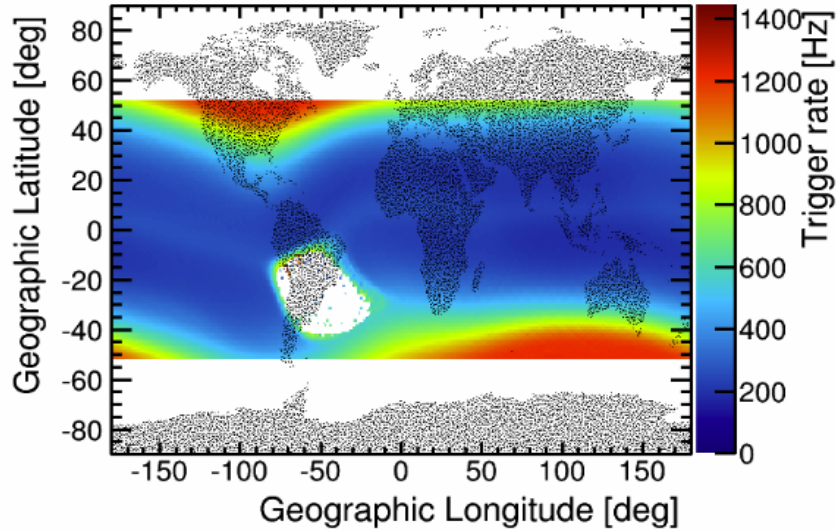
Figure 3.11: AMS-02 event rate in Hertz plotted for geographic latitude and longitude. The blank spot around the South Atlantic Anomaly is due to the vetoed data because of the high rate of events in that region [14].

Data acquisition is performed onboard the International Space Station and the data analysis starts on the ground at the POCC. A key parameter in the analysis is livetime

of the the detector which is the fraction of time in which a new event can trigger the readout of the AMS-02 detector. The blank spot around the South Atlantic Anomaly in Figure 3.11 shows the vetoed data because of the high rate of events in that region.

The POCC contains 5 different monitoring consoles for different subdetector operations and data acquisition.

• Lead desk: Apart from commanding, data acquisition, communication with NASA and detector operations are performed.

• Data desk: Data received and stored are controlled.

• Thermal desk: Temperature sensors are monitored whether their values are inside in healthy intervals or not.

• PMT desk: Monitoring physical parameters of RICH, TOF and ECAL, such as temperature, number of signals and current process, are performed.

• TT desk: Monitoring physical parameters of TRD, Tracker and ACC, temperature, number of signals and current process, are performed.

Everyday 24 hours monitoring, divided by three eight-hour shifts, is being carried out at POCC.

Chapter 3 detailed instrumentation parts of the AMS-02, reconstructions, monitoring and data acquisiton. For the proton analysis, charge measurements from the TOF, the Tracker vs rigidity graphs and beta vs rigidity graphs are important. After getting these graphs for both data recorded by the AMS-02 and Monte Carlo simulations, proton flux measurement will be performed.

36

CHAPTER 4

MEASUREMENT OF THE PROTON FLUX

The precise measurement of the proton flux in cosmic rays can help clarify interpretations of mechanisms of production, acceleration and propagation of cosmic rays. Among charged particles, protons are the most abundant particles above the GV rigidity level. The measurement of the proton flux for rigidities from 1 GV to 1.8 TV based on 30 months of AMS-02 data was presented in a paper published in 2015 [16].

In this chapter, proton flux measurement based on 5 years of AMS-02 data will be given. A cut-based analysis is performed in the GV-TV (least resolution effect in the interval) rigidity region with a study of systematic errors. The key instruments used in this measurement are the Tracker and the Time of Flight detectors. The analysis begins with the identification of protons. Monte Carlo simulation is then the next step of analysis in order to obtain an effective acceptance, which is the normalization of events that takes the geometric acceptance into account as well as corrections that arise from possible discrepancies between simulation and data. Proton flux calculation is finally performed and crosschecked with the published results.

4.1   Proton Identification with AMS-02

For the first 5 years of AMS-02 data, the proton flux measurement is performed based on 5.6×10^8 events. The data collection time only includes a fraction of the time when the detector was in normal operating conditions. The collection time changes up to 30 GV. Since protons with a rigidity higher than 30 GV are no longer under geomagnetic-cutoff, the collection time stabilizes to 1.2×10^8 second. Because of the geomagnetic cutoff effect, the South Atlantic Anomaly (SAA) is dominated by charged particles.

Therefore a high event rate in a small fraction of time may lead to misreconstructed events in the detector in the SAA. For this reason, AMS-02 data recorded in the SAA are not used in the analysis. To select primary cosmic rays, particle rigidity is required to be greater than 1.2 times of the geomagnetic cutoff, as calculated by backtracing. Backtracing is an algorithm which can help to determine a particle's origin of Earth radii by using magnetic field lines equations. And the geomagnetic cutoff in terms of rigidity is given by Stömer approximation using dipole field, and is given in Equation 4.1 [15]. In geomagnetic model, there is a safety factor to avoid uncertainties. Safety factor is determined as 1.2 in the proton flux measurement.

$$R_c = \frac{M cos^4\lambda}{r^2(1 \pm \sqrt{1 - sin\epsilon sin\xi cos^3\lambda})^2} \tag{4.1}$$

where M is the magnitude of the dipole moment, λ is the latitude from the magnetic equator, ϵ is the zenith angle of the incoming particle, ξ is azimuthal angle to the north magnetic pole and r is the distance from the dipole center. Lastly the sign of the charged particle is taken into account in the formulation as well. If charge of a particle is a positive sign, $\pm$ term is taken as a positive, and vice versa. The Figure 4.1 shows backtracing processes with different rigidities around Earth. Number one represents the highest rigidity and the last one, labeled as 15, represents lowest rigidity. Given the structure of the magnetic field, International Geomagnetic Reference Field (IGRF) [78], the backtracing algorithm traces a charged particle from top of AMS-02 out to 50 Earth's radii [79].
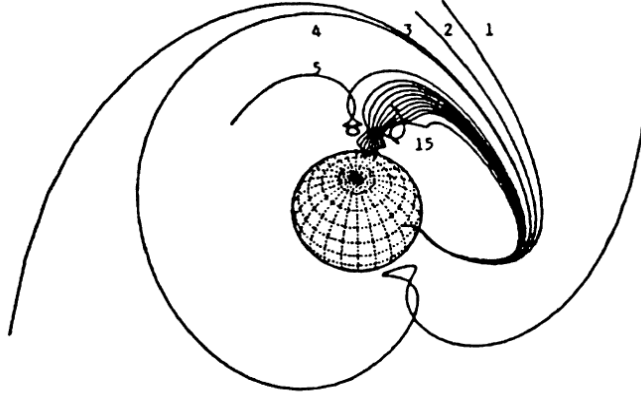
Figure 4.1: Examples of backtracing process with different rigidities. Number one represents the highest rigidity and the last one, labeled as 15, represents lowest rigidity [15].

Furthermore, the incident angle of selected events is restricted to within $25°$ of the local zenith of the AMS-02 to compute an effective acceptance of protons by the detector. Purpose for this selection is to make a full span analysis (signal for both first and last layer of the Tracker) for proton flux measurement. Livetime is a fraction of each second to record a new event. The corresponding livetime for the data acquisition is also determined to exceed %50 to avoid misconstructed events in high event rates.

Tracker and TOF play a main role in the identification of protons. Tracker is the key instrument of the AMS-02 to measure charged particles among cosmic rays. While the charge measurement for the first and last layer of the Tracker is between 0.6 and 1.9 (number of proton), protons are required to have a charge in 0.7-1.5 interval for the inner layers. For proton measurement, particles are required to have a track in both the first and the last layers of the Tracker, referred to as full span selection. Further selections are made by demanding the track passes $2\&(3 \parallel 4)\&(5 \parallel 6)\&(7 \parallel 8)$ layers of the Tracker. Another cut regarding the Tracker signal is $\chi^2/d.o.f.$, which shows how good track fitting is for the analysis and events with a value less than 10 are accepted in this analysis. The full span rigidity requirement is $1/fullspanrigidity <$

1/0.8 [16]. Here full span means rigidity reconstruction from information of tracker including first and ninth layers.

The second important instrument in the proton identification is the Time of Flight detector since the reconstruction of beta (v/c) is provided by the data taken by the detector. For this proton analysis, beta is required to be greater than 0.3. Charge of the particle can be reconstructed by TOF as well. The selection criteria for the charge measurement is between 0.5 and 3 for lower TOF. The cuts are determined in order to decrease systematic error contributions as low as possible.

4.2 Definition of Flux and Related Variables

The isotropic proton flux ϕ_i in the rigidity bin in between R_i and $R_i + \Delta R_i$ is given in unit GV^{-1} m^{-2} sr^{-1} s^{-1} as

$$\phi_i = \frac{N_i}{A_i \epsilon_i T_i \Delta R_i} \tag{4.2}$$

where N_i is the number of events, A_i is the effective acceptance, ϵ_i is the trigger efficiency and T_i is the collection time. The measurement of each of these parameters will be detailed in following sections. This proton analysis which ranges from 1 GV to 1.8 TV is performed using 72 logarithmic rigidity bins. The main purpose of using logarithmic scale for the rigidity abscissa is to see the power law behaviour of the proton flux in detail. Moreover data belonging to this interval are collected between July 2011 and May 2016.

4.3 Measurement of Variables Required for the Proton Measurement

4.3.1 The Collection Time for Protons

The collection time, also called the exposure time, is the effective time in which the detector is in normal operation conditions. In other words, time spent on readout system, data acquisition, ISS docking or undocking, TRD gas refill are taken

into account in order to obtain the effective operation duration of the detector and subtracted from operation time of the AMS-02 for flux measurements. The only way to assess each second of data collection time is the Real Time Information class included in AMS-02 Offline software.
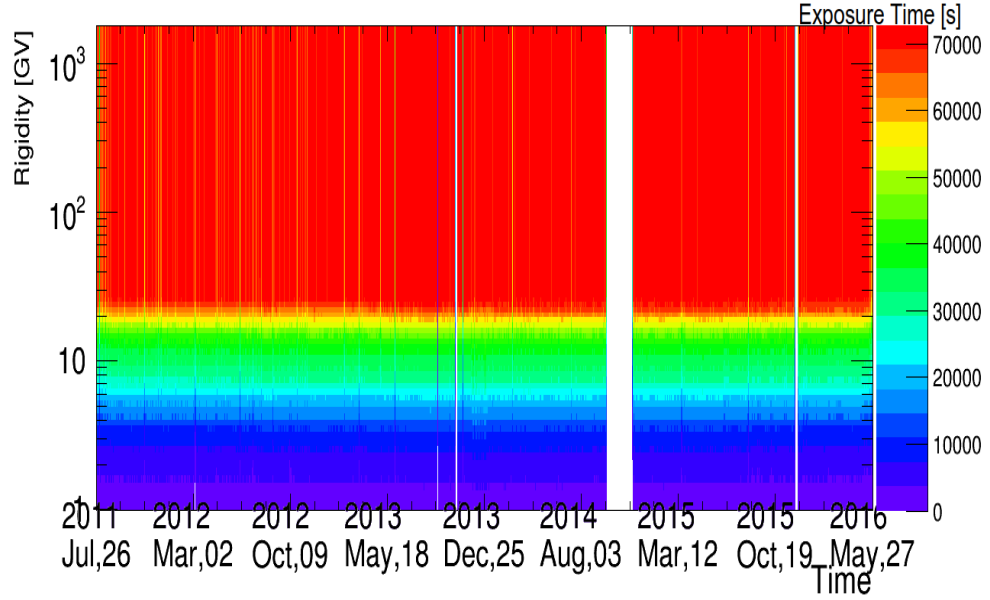
Figure 4.2: Exposure time (s) of the AMS-02 versus particle rigidity and data collection date. The blank period in 2014 is the period when the detector was temporarily out of operation due to recovery operations and calibrations after the shut down of the Tracker Thermal Cooling System.

Only if the conditions listed below are satisfied, the exposure time of the AMS-02 is evaluated as a function of data collection date and positive rigidity, shown in Figure 4.2. The colors represent exposure time of the measurement.

• Livetime is greater than 0.5 s

• The detector z-axis is pointing within $25°$ of the local zenith

• Bad runs, namely misconstructed events, are removed

• Events measured in the SAA are removed

The blank part of exposure time graph represents the period, when the detector was

41
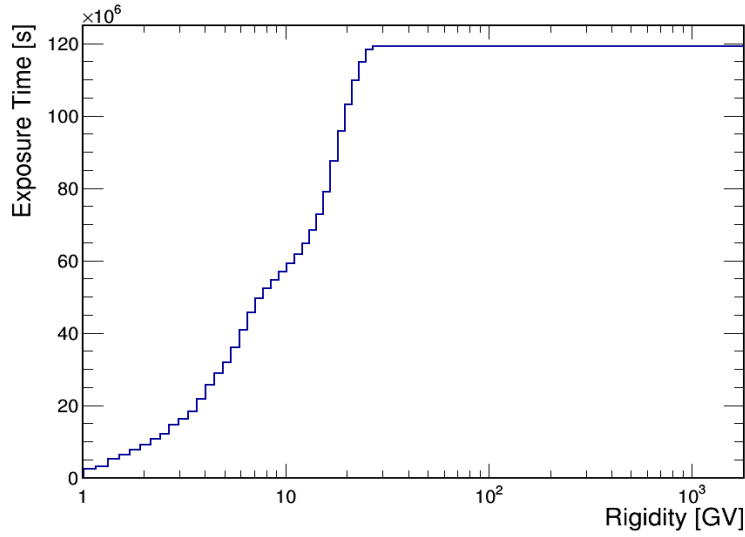
Figure 4.3: Exposure time versus rigidity. It rises up until 30 GV after which it stays constant roughly at 1.2 times 10^8 s.

out of operation since the pump in the tracker thermal cooling system was off during that interval. At the same time, some operational tests were also performed to improve calibrations and performance of the detector.

Rigidity versus exposure time can be seen in Figure 4.3. Due to the geomagnetic cutoff effect, the exposure time increases with rigidity until 30 GV over which it is no longer rigidity dependent and stays constant at almost 1.2×10^8 s.

4.3.2 Trigger Efficiency for Protons

The trigger system is dependent on the trigger signal combination provided by the TOF, the ACC and the ECAL. Different particles have different fast trigger mechanisms due to their mass and charge but also dependent on their velocity. These are for charged particles, slow particles with high mass and neutral particles. The signal produced after processing in the pre-determined mechanism is sent to a dedicated electronics board called JLV1 [63].

The trigger efficiency is measured with with respect to unbiased trigger and is calcu-
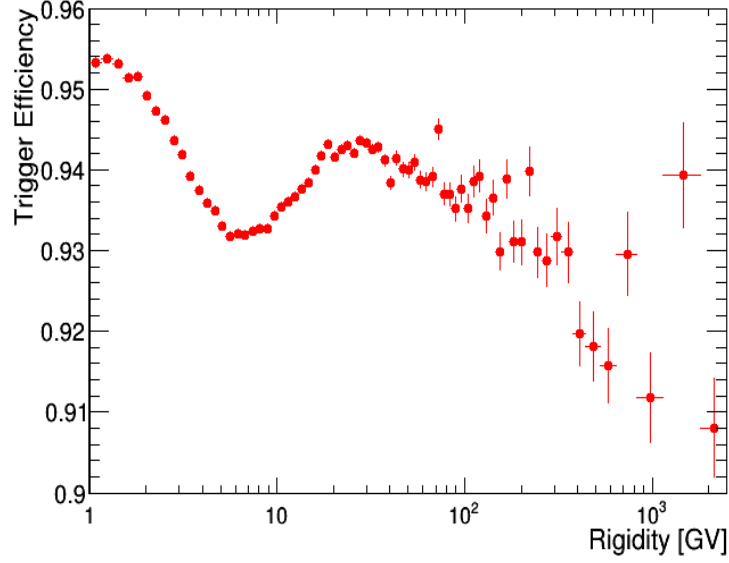
Figure 4.4: The trigger efficiency versus rigidity

lated by,

$$\epsilon_{trigger} = \frac{N_{triggered}}{N_{triggered} + f_{prescale} \times N_{unbiased}} \tag{4.3}$$

where $f_{prescale}$ is the prescale factor which equals to 100. In other words, it means that only 1 in 100 events is taken as a unbiased event in the data acquisition system. $N_{triggered}$ is obtained after applying necessary cuts explained in the section 4.1. The reason for 100 is to not to overload system for the tigger system. The Figure 4.4 shows the trigger efficiency versus rigidity. The trigger efficiency varies in the range between %91 and %95. The secondary γ rays entering to the ACC result in this small inefficiency.

4.3.3 Effective Acceptance for Protons

The first part of normalization for the flux is an effective acceptance ($A_{eff}(R)$) in units of m^2sr where the geometric area, correction for the selected subdetectors and selection efficiency are taken into account, as shown in Equation 4.4.

$$A_{eff}(R) = A_{geom}(R) \cdot [1 + \delta(R)] = G \cdot \epsilon_{sel}(R)[1 + \delta(R)]$$
$$= G \frac{N_{sel}(R)}{N_{gen}(R)}[1 + \delta(R)]$$
$$= G \frac{N_{sel}(R)}{N_{gen}(R)}\kappa(R) \qquad (4.4)$$

The initial part of obtaining an effective acceptance is a calculation of geometric acceptance (A_{geom}) related to event reconstruction and selections. At first, the geometric factor (G) is evaluated with a sample of simulated protons distributed over a generation surface and multiplied by selection efficiency that will be detailed in following section. Then the geometric acceptance is corrected with a correction term $[1 + \delta]$ representing correction for any discrepancies between the data and MC simulation. The procedure is applied for each cut in the event selection and $\kappa_i(R)$ is given as,

$$\kappa_i(R) = \frac{\epsilon_{i,data}(R)}{\epsilon_{i,MC}(R)} \qquad (4.5)$$

where $\epsilon_{i,data}(R)$ is efficiencies for each cut obtained from AMS-02 data and $\epsilon_{i,MC}(R)$ is efficiencies for each cut obtained from MC simulation.

4.3.3.1 Geometric Acceptance for Protons

The geometric acceptance is a calculation where the geometric factor and selection efficiency are taken into account. The key process calculating this acceptance is a Monte Carlo simulation. The determining parameters for the counting rate of any particle-detecting instrument are their effective dimensions and relative positions for a given energy interval. First of all, the geometric factor is evaluated with Equation 4.6 [80],

$$G = \int_{\omega} d\omega \int_{S} d\sigma \cdot \hat{r} = \int_{\omega} \int_{S} cos\theta d\sigma d\omega = \int_{S} \int_{0}^{2\pi} \int_{0}^{\pi/2} \cos\theta \sin\theta d\theta d\phi d\sigma$$
$$= 2\pi S \int_{0}^{1} \cos\theta d(\cos\theta) = \pi S \qquad (4.6)$$

where $d\sigma$ is the surface area element, S is the corresponding surface area and $d\omega$ represents element of solid angle including polar angle the θ and the azimuthal angle ϕ respectively.

In this case the event-generation plane is a concentric cube with 3.9 m length for each side. The MC simulated events are generated isotropically on the top plane of the cube, shown in Figure 4.5. Therefore the geometric factor, $\pi \times 3.9m \times 3.9m$, is equal to approximately 47.78 m^2 sr.
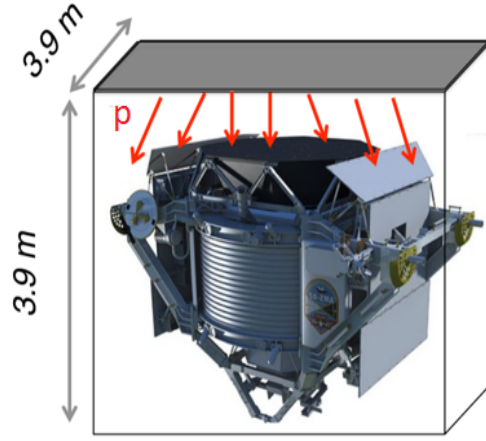
Figure 4.5: The concentric cube around AMS-02 for the generated MC events. Each side has 3.9 m length and events are generated isotropically from the top plane of the cube.

Second, the calculated geometric factor is multiplied with fraction of triggered particles and generated particles, given in Equation 4.7

$$A_{geom}(R) = G\epsilon_{sel}(R) = G\frac{N_{trig}(R)}{N_{gen}(R)} \tag{4.7}$$

Finally, the acceptance versus true rigidity is given in Figure 4.6. True rigidity is the generated rigidity assigned for each event in the Monte Carlo simulation.

At low rigidity, AMS-02 magnetic field, absorption in the material, survival probability and trigger efficiency effect the geometric acceptance while at high energies, the small deviations are because of the Monte Carlo structure.
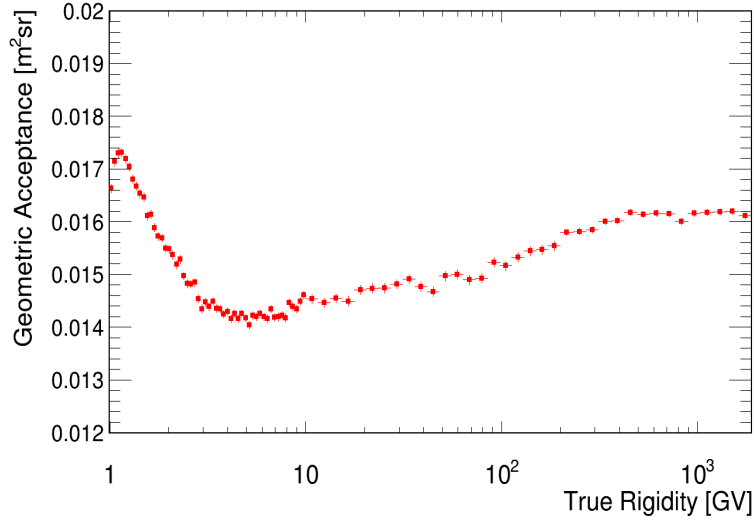
Figure 4.6: The geometric acceptance of AMS-02 versus true rigidity as generated by the Monte Carlo simulation.

4.3.3.2 Correction Multiplication for Protons

Third term in Equation 4.4 is the multiplicative factor related to the subdetectors chosen for event reconstruction and event selection so that the systematic discrepancy between data and simulation is calculated. The calculation is performed with the inner Tracker (L2-L8), the external Tracker (L1 and L9) and the Time of Flight detector separately.

The idea in order to obtain a systematic discrepancy for each of the detectors is to create a pure sample of protons by using the other subdetectors measurements and reconstructions. And then this sample is sent to the related subdetector efficiency of which is wanted to be calculated. For instance, a clean sample of proton is first reconstructed by the Tracker then this sample is used to see how efficient the TOF is to record protons in its signal acquisition system. The requirements for the TOF event selection are given below;

• Beta pattern is less than 5. That means taking only events that have hits on 3 or 4 TOF layers.

- Beta is bigger than 0.3

- Charge measured in lower TOF layers is between 0.5 and 3

- TOF clusters in time is less than 4. That means requiring number of hits on TOF layers is less than 4

The resulting efficiencies for simulation and data and their ratio (lower panel) are presented in Figure 4.7. In the upper panel blue markers represent TOF efficiency for simulation while the red markers represent the one for data. While the efficiency for proton data is more than 99 %, the efficiency for simulation includes some deviations, seen in the upper panel of the figure, especially at high rigidity due to Monte Carlo statistics and structure which will be detailed at external tracker efficiency part. The bottom panel shows the ratio of Data and MC.

Figure 4.7: TOF efficiencies for simulation and for data (upper panel) and their ratio (lower panel) versus reconstructed rigidity from the Tracker. In the upper panel blue markers represent TOF efficiency for simulation while the red markers represent the one for data. And the green markers give the ratio of them in the bottom panel.

Next possible systematic efficiency discrepancy calculation is performed for the External Tracker which represents first and last layers of the Tracker. After reconstructing a pure sample using the TOF and the Internal Tracker, the External Tracker efficiencies are calculated for both simulation and data. The selection criteria for the External Tracker efficiencies is listed below,

• A tight charge cuts for first and last layer are $0.6 < Z_{L1} < 1.9$ and $0.6 < Z_{L9} < 1.9$

• χ^2 is less than 10

• XY hit on both L1 and L9 layers

External Tracker for simulation and for data (upper panel) and their ratio (lower panel) versus reconstructed rigidity from the Inner Tracker is shown in Figure 4.8.

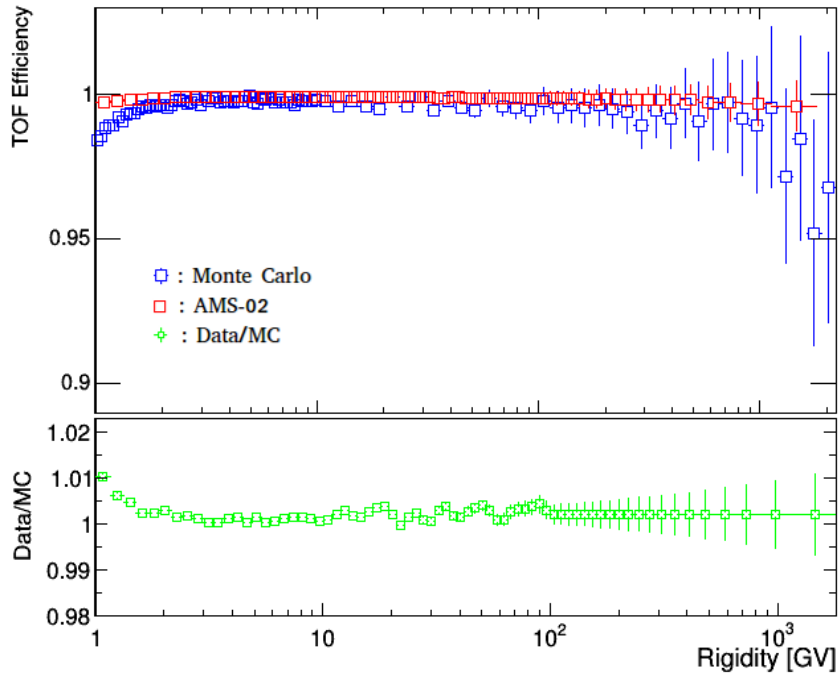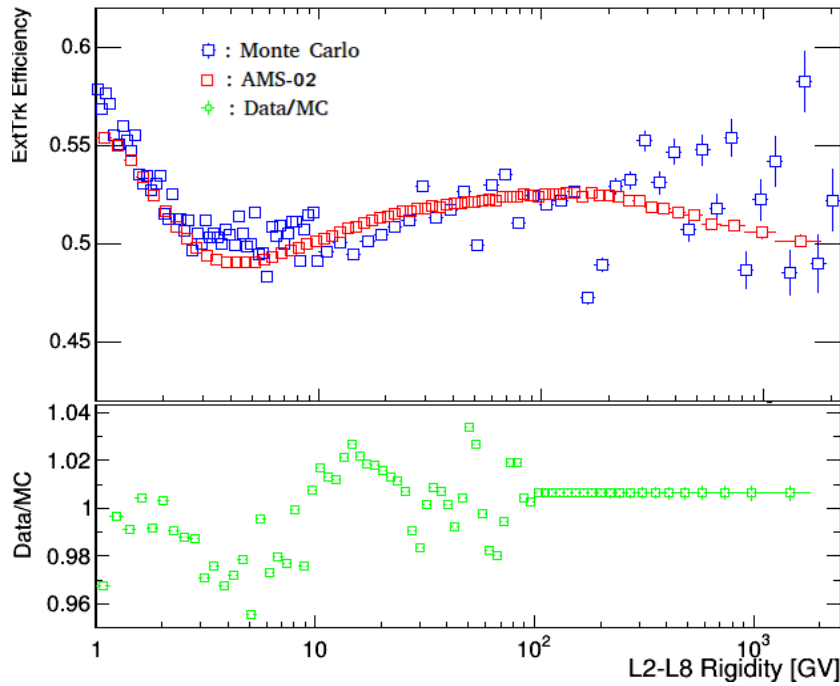Figure 4.8: External Tracker for simulation and for data (upper panel) and their ratio (lower panel) versus reconstructed rigidity from the Inner Tracker. In the upper panel blue markers represent the External Tracker efficiency for simulation while the red markers represent the one for data. The External Tracker efficiencies take value around 0.6 since it only includes first and last layer of the Tracker.

In the upper panel blue markers represent External Tracker efficiency for simulation while the red markers represent the one for data. Even though the External Tracker efficiencies for simulation and data are very close to each other, they take a value between 0.5 and 0.6 for all reconstructed rigidities. The reason is that the survival probability decreases until reaching both external layers of the Tracker. However, the bottom panel clearly shows the agreement between MC and data is within %5. In addition to statistics error contributions in MC simulation, the reason for deviations is due to the fact that MC does not correctly reproduce all particle interactions especially for low and high rigidities where the importance of the material in the detector is relevant.

Finally the possible systematic discrepancy for the Inner Tracker is a challenging progress because rigidity reconstruction without magnetic field. Normally, the rigidity is reconstructed with the contributions of the permanent magnet and inner layers of the Tracker. However, without their information, the rigidity only can be obtained using different variable as an alternative estimator in the rigidity range of [1-7] GV. The estimator of the rigidity, beta, from the TOF is converted to rigidity using Equation 4.8. For this measurement the rigidity is equal to momentum of the particle with theoretical approach since charge of the selected particle, the number of proton, is determined as 1. The conversion between beta and rigidity is started using the relativistic energy of the particle, defined as,

$$E^2 = p^2 c^2 + m^2 c^4 \Rightarrow R^2 = m^2(\gamma^2 - 1)c^2 \tag{4.8}$$

γ is then replaced with $\sqrt{\frac{1}{1-\beta^2}}$ and the equation takes its final form, given in Equation 4.9.

$$R = \frac{m\beta}{\sqrt{1-\beta^2}}c \tag{4.9}$$

The conversion is valid only up to ~ 8 GV since estimated rigidity is limited by the TOF β resolution. The selection criteria for Inner Tracker efficiency is given as;

• At least one hit at L2 & (L3 ‖ L4) & (L5 ‖ L6) & (L7 ‖ L8)

49
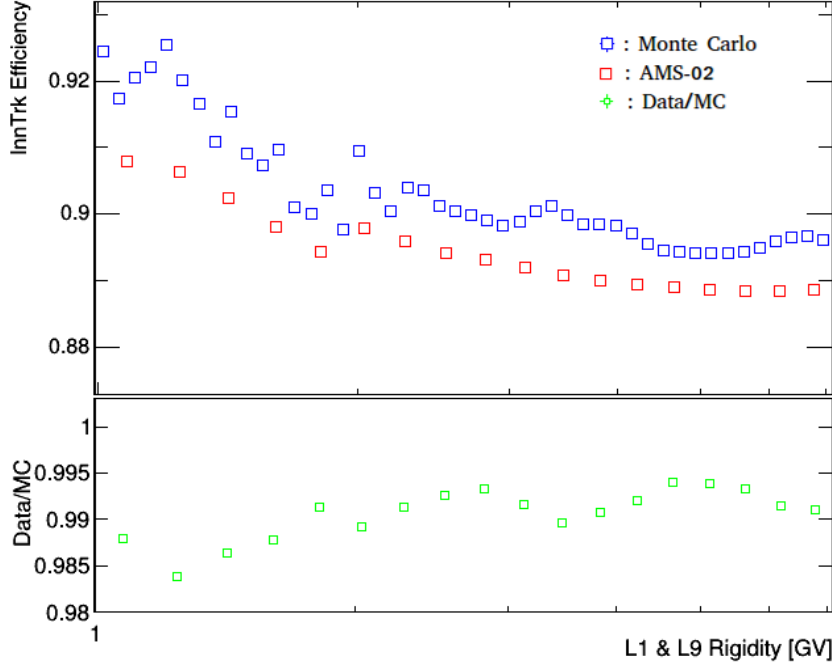
Figure 4.9: Inner Tracker efficiencies for simulation and data (upper panel) and ratio of the efficiencies (lower panel) versus reconstructed rigidity from the External Tracker. In the upper panel blue markers represent the Inner Tracker efficiency for simulation while the red markers represent the one for data. The analysis was performed up to 7 GV because of beta resolution.

- Inner charge is between 0.7 and 1.5

The Figure 4.9 shows the Inner Tracker efficiencies versus reconstructed rigidity from the External Tracker (upper panel) and ratio of the efficiencies from the data and the simulation (lower panel). Although there is a good agreement between data and MC, the values are only valid up to 7 GV due to beta resolution.

4.3.3.3 Corrected Acceptance

After standalone efficiencies for each subdetector determined in the reconstruction, the correction for possible systematic discrepancies and AMS-02 geometric acceptance are combined in the corrected effective acceptance, shown in Figure 4.10. The equation 4.4 includes all the environmental conditions, electronics systematics as

50

modelled by Geant4, survival possibilities and extrapolations in order to retrieve the real value of the incident proton flux.
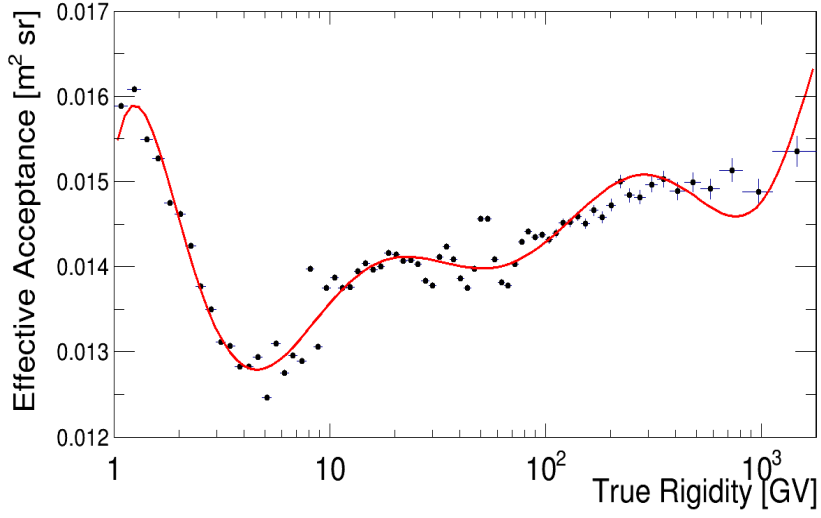
Figure 4.10: The corrected effective acceptance versus true rigidity. The fit is extrapolated from a polynomial function which is set with parameters obtained in root.

The suitable fit comes from the polynomial function which is extrapolated as a function of true rigidity and given as;

$$[0] + [1] \times log_{10}x + ([2] \times \sqrt{log_{10}x}) + ([3] \times log_{10}x^3) + ([4] \times log_{10}x^4) + ([5] \times log_{10}x^5)$$
$$+([6] \times log_{10}x^7) + ([7] \times log_{10}x^8) + ([8] \times log_{10}x^9)$$

(4.10)

4.4 Proton Flux Measurement

Using Equation 4.2, the proton flux measurement is obtained in unit of m^{-2} sr^{-1} s^{-1} GV^{-1}. The measured proton flux, ϕ, is for rigidities from 1 GV to 1.8 TV with total errors including the quadratic sum of the statistical and systematic errors. The contributions to the systematic errors are rigidity and beta resolution, event selection, the trigger, the acceptance especially Monte Carlo structure modelled by Geant4, geo-

51

magnetic cutoff factor and background contamination especially deuterons. However protons among cosmic rays are so abundant that the deuterons contamination is not strong case to be accounted for. In Figure 4.11, the proton flux measurement is shown and also compared with AMS published proton result from 1 GV to 1.8 TV. The black line represents the published proton flux measurement. The flux decreases with the spectral index 2.7, also detailed in Chapter 2, which is defined as:

$$\gamma = \frac{d[log(\phi)]}{d[log(R)]} \tag{4.11}$$

The proton flux is multiplied by $\tilde{R}^{2.7}$ to see proton flux in detail especially at low and high rigidities where the resolution effects are more relevant. The multiplied result is shown in Figure 4.12 compared with the AMS published proton measurement [16] and their ratio is given in bottom panel. For low and high rigidities the ratio is not consistent with total quadratic and systematical error bars obtained from published result. It is due to lack of an unfolding procedure which will be applied in the next section to correct for effect of finite rigidity resolution.
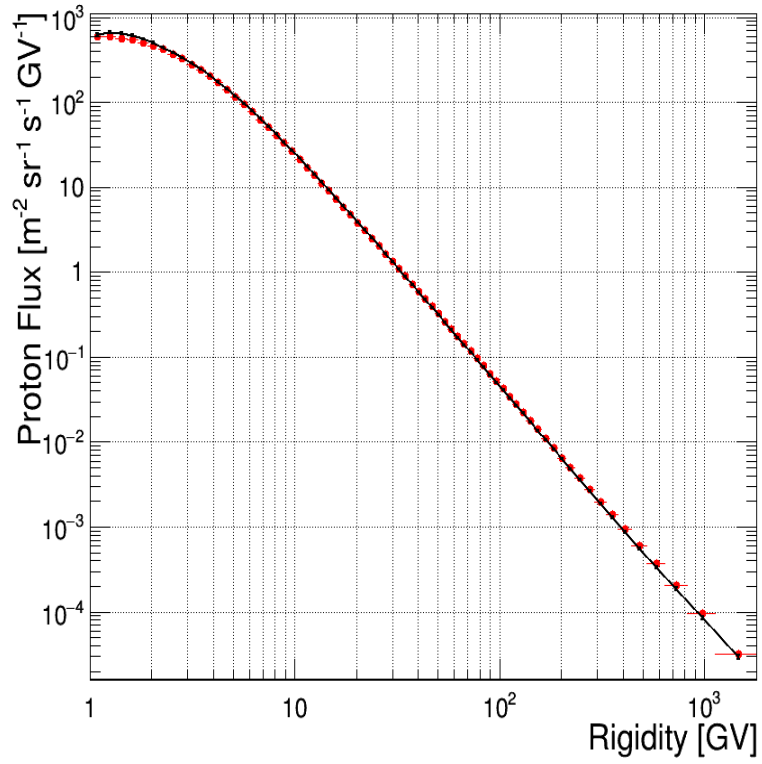
Figure 4.11: The measurement of proton flux versus rigidity. The proton flux (red markers) is presented along with the AMS published proton flux measurement (black line) [16]. Error bars on proton flux are so small in log scale that it is cannot be seen here. For example for the last bin, the error bar is 1.6×10^{-7}. Unfolding is not taken into account.

Figure 4.12: The measurement of proton flux multiplied by $\tilde{R}^{2.7}$ versus rigidity. The upper panel shows the multiplied proton flux measurement compared with the AMS-02 published proton flux measurement (black line). The bottom panel gives the ratio of this proton flux measurement and the AMS-02 published proton measurement [16]. The ratio has big deviations which are not consistent with total quadratic and systematic errors from published one especially at very low and high rigidities because unfolding is not taken into account.

4.5 Unfolding Procedure

The procedure in which energy resolution effects are corrected with different techniques is called unfolding. Two techniques used for AMS analyses are based on bin to bin correction. Both techniques are verified with a Monte Carlo simulation. The first method uses the ratio between the number of events falling in a certain bin of a reconstructed variable and the number of events in the same bin of the generated variable from the simulation. This procedure is applied after flux is obtained without rigidity resolution function is taken into account [81]. The second way, applied in this analysis uses the migration matrix where a set of spline functions with different node positions is used [82]. Unlike the first way, this technique is performed while the necessary parameters for proton flux are being calculated.
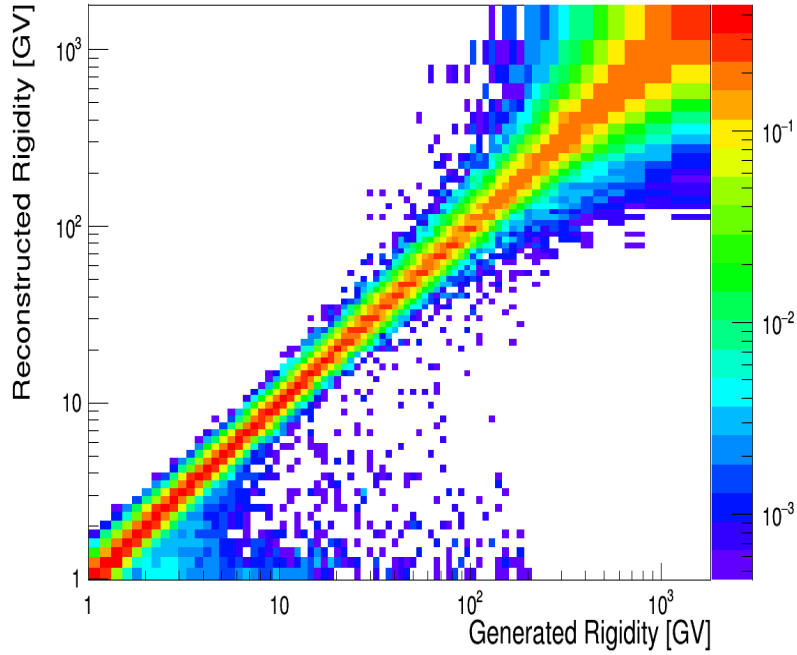
Figure 4.13: The migration matrix plot. The x-axis is the generated rigidity obtained from simulation. The y-axis is reconstructed rigidity obtained from AMS-02 data. The color scale represents relative counts.

The Figure 4.13 shows reconstructed vs generated rigidity to obtain migration matrix so that the resolution effects of the detector are corrected. At high rigidities the width

is because of resolution of the Tracker. It is a pure effect of curvature measurement. Given the tracker spatial resolution, at high rigidity, it gets more and more difficult to state if a particle is bending or not. At low rigidities, on the other hand, the spread in terms of relative counts represents energy loss in passive material that is hard to reconstruct properly. Moreover, multiple scatterings and misreconstructions that are not recorded by the ACC result in fake distributions in the plot. In this way, for each bin the reconstructed rigidity is migrated to generated rigidity without losing relative count for the measurements.

Figure 4.14 shows the proton flux measurement along with the AMS-02 published measurement after unfolding method is applied. In order to see how the unfolding procedure affects especially at low and high rigidities, Figure 4.15 is given with ratio of this work and the published measurement (bottom panel).
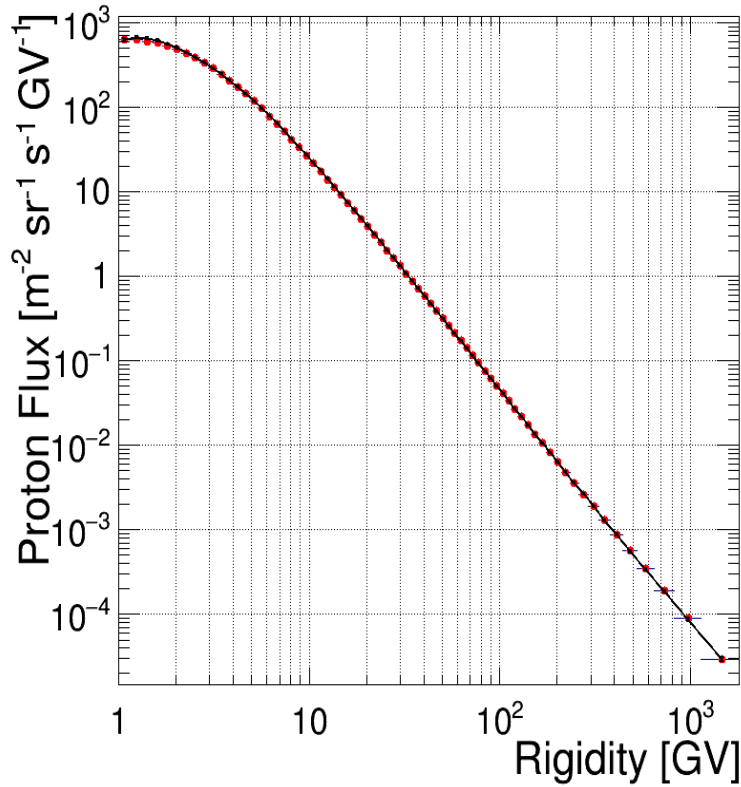
Figure 4.14: The measurement of the unfolded proton flux versus rigidity. The unfolded proton flux (red markers) is presented along with AMS-02 published proton flux measurement (black line) [16].
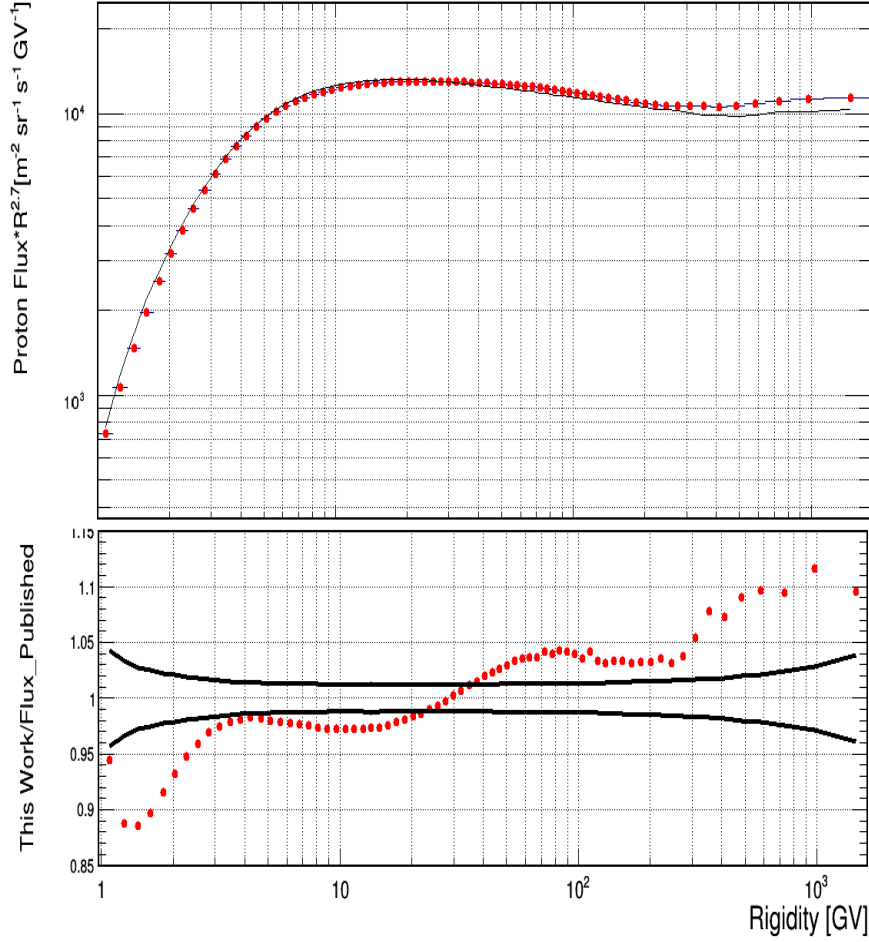
56
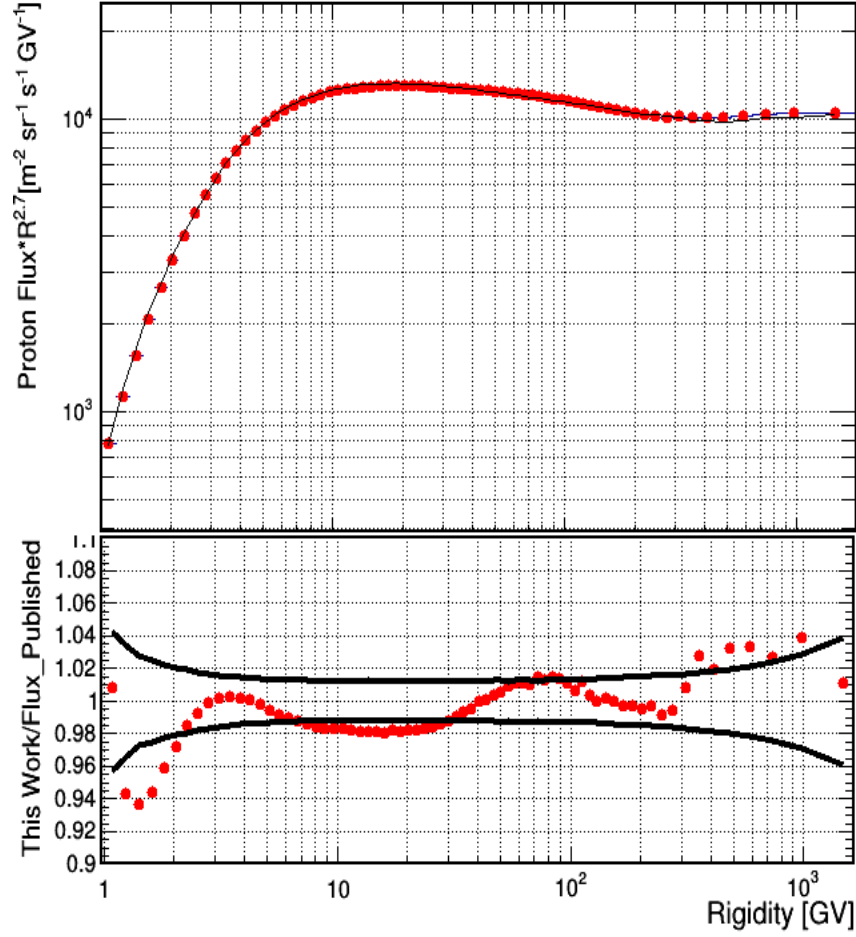
Figure 4.15: The measurement of the unfolded proton flux multiplied by $\tilde{R}^{2.7}$ versus rigidity. The upper panel shows the multiplied proton flux measurement compared with the AMS-02 published proton flux measurement (black line). The bottom panel gives the ratio of this unfolded proton flux and the AMS-02 published proton measurement. The ratio is inside the total quadratic and systematic errors from published one.

4.5.1 Comparison of the the AMS-02 Measurement with SPENVIS Predictions for ISS in Earth's Vicinity

Space ENVironment Information System (SPENVIS) provides several models for the space environment through a World Wide Web interface. Rapid analyses are made for radiation belts, solar energetic particles, cosmic rays, plasmas, gases, magnetic fields and micro-particles with SPENVIS. The working principle of SPENVIS is based on a spacecraft's trajectory or coordinate grid. After defining either of them, radiation sources and effects can be analyzed for the defined orbit by using SPENVIS.

In this analysis, within 5 years of mission duration, International Space Station perigee and apogee are defined as 403 and 406 respectively as input parameters. Also 11 July 2011 is defined as initial time input. The model used in the analysis is ISO 15390 which includes international standarts.

Figure 4.16 shows the comparison of the AMS-02 proton flux measurement with the SPENVIS as a function of kinetic energy. The comparison is shown up to 100 GeV because SPENVIS only gives the flux up to this energy. Fluxes show differences. As clearly seen from the figure, SPENVIS flux predictions are lower than the proton flux measurement performed with AMS-02 data after ~ 2 GeV. SPENVIS provides a flux prediction using the worst case scenario for the Sun. However AMS-02 proton flux measurement gives the observed events along the orbit. Bottom panel shows ratio of proton flux measurement and SPENVIS predictions. At some energies since SPENVIS predictions cover 10 GeV kinetic energy range, the flux decreases with order.

Many models for cosmic ray origin, propagation and acceleration detailed in Chapter 2 require an rigidity dependence with a spectral index changing between 2.7 and 3. Moreover protons are abundant among other cosmic rays above $\sim$ GV. The proton flux measurement performed in this thesis approves the spectral index dependence as approximately 2.7 with 5 years of the AMS-02 data. The proton flux measurement is compared with the AMS-02 published proton flux measurement. That shows abundance of protons among other cosmic rays when they are compared with other AMS-02 published cosmic ray measurements detailed in Chapter 1. In the last part
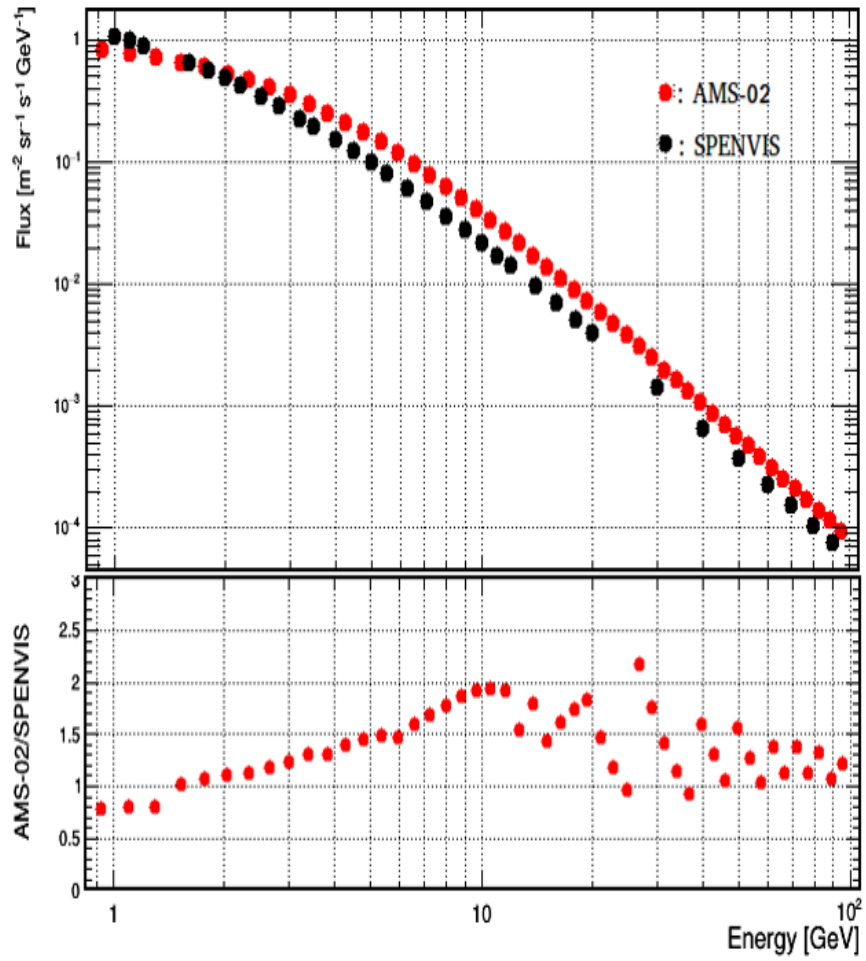
Figure 4.16: The comparison of the AMS-02 proton flux measurement (red markers) with the SPENVIS predictions (black markers) versus kinetic energy. The comparison is shown up to 100 GeV because SPENVIS only gives the flux up to this energy. Both at low and high energies, fluxes show differences. The difference on flux is because SPENVIS predictions take worst-case scenarios of the Sun into account. Bottom panel shows ratio of proton flux measurement performed with AMS-02 data and SPENVIS predictions. At some energies since SPENVIS predictions cover 10 GEV energy the flux decreases with order.

59

of the chapter, the comparison between the proton flux measurement and SPENVIS predictions shows similar results for kinetic energies from 1 GeV to 100 GeV. Since SPENVIS predictions are based on worst-case scenarios for the Sun, the integrated flux differs from the proton flux measurement performed with the AMS-02 data.

In the following chapter, the analysis will contain proton flux measurement variability in time to observe solar modulations caused by solar activities. The time dependent proton flux measurement especially at low rigidities will be performed to understand solar wind and coronal mass ejections effects at LEO. The 11-year solar cycle effects of the Sun, detailed in Chapter 2, will be analyzed for characteristic bins.

CHAPTER 5

PROTON VARIABILITY IN LOW EARTH ORBIT

The 11-year solar cycle, where the number of sunspots decreases reach a minimum and then increases to a maximum then goes back to a minimum again causes solar activities. These solar activities lead to a modulation of the cosmic ray intensity in the heliosphere. With large acceptance and exposure time, AMS-02 provides a unique opportunity to probe the dynamics of solar modulation on board the International Space Station [28].

The precision measurement of the proton flux for 69 Bartels rotations will be presented in this chapter. Bartels rotation is a 27 days period which lets track certain recurring or shifting patterns of solar activities. The proton flux measurement is based on 5.6×10^8 events. In addition, a time dependent unfolding procedure was applied to the proton flux measurement in order to correct the rigidity resolution effect.

5.1 Definition of Time Dependent Flux and Related Variables

The isotropic proton flux ϕ_i for each Bartels rotation in the rigidity bin in between R_i and $R_i + \Delta R_i$ is given as

$$\phi_i = \frac{N_i}{A_i \epsilon_i T_i \Delta R_i} \tag{5.1}$$

where N_i is the number of events, A_i is the effective acceptance, ϵ_i is the trigger efficiency and T_i is the collection time. The time dependent parameters will be detailed in the following sections.

5.1.1 Time Dependent Collection Time

The time independent collection time differs from the time dependent one in terms of binning process. In this concept of exposure time, the time scale is divided into 69 Bartels rotation periods [83] between 11 June 2011 and 2 November 2016. The Figure 5.1 shows operation time versus rigidity for 69 Bartels rotations. The change up to 30 GV is because of the changing geomagnetic rigidity cut-off. Given the precise location of the detector inside the magnetic field of the Earth, particles which have rigidity bigger than this rigidity cut-off are recorded as triggers in the detector. The blank period is the time when the detector was out of operation due to recovery and operations after the shut down of the Tracker Thermal Cooling System.
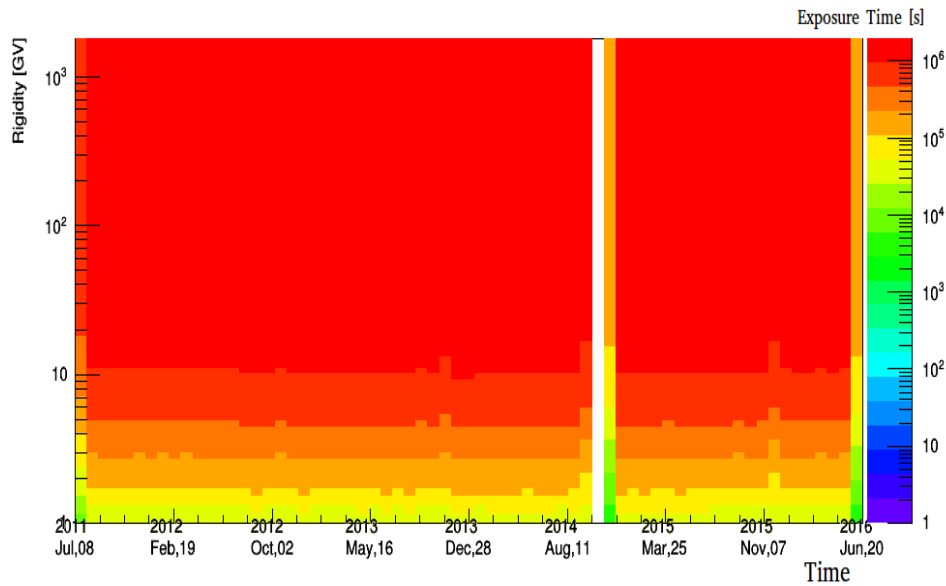
Figure 5.1: Exposure time of the AMS-02 versus rigidity and operation time for 69 Bartels rotations. The x-axis gives operation time of the AMS-02, y-axis gives measured rigidities and the color scale gives exposure time in seconds. The blank period is the time when the detector was out of operation due to calibrations and operations after the shut down of the Tracker Thermal Cooling System.

5.1.2 Time Dependent Trigger and Subdetector Efficiencies

Effective acceptance, given in Equation 4.4, calculation includes a time dependent $1 + \delta$ factor which is shown in Equation 5.2. The factor is obtained as;

$$1 + \delta = \kappa_{Data(t)/MC} = \kappa_{Data(t)/Data} \cdot \kappa_{Data/MC} \qquad (5.2)$$

Where $\Pi_{Data/MC}$ was obtained in Chapter 4 and $\Pi_{Data(t)/Data}$ represents time dependent discrepancy between from data and MC simulation for each cut related with subdetectors used in proton flux measurement. Figure 5.2 shows fraction for each cut between data and MC for rigidity bin interval 4.88-5.37 GV for the 38th Bartels rotation between 6 March and 2 April 2014. This process was repeated for each Bartels rotation over the whole GV-TV rigidity range.

The Figure 5.3 shows the overall data(t)/data efficiency between 6 March and 2 April 2014. It includes time dependent efficiencies for rigidity bin interval 4.88-5.37 GV and for each cut performed in related subdetector and also trigger system for the 38th Bartels rotation.
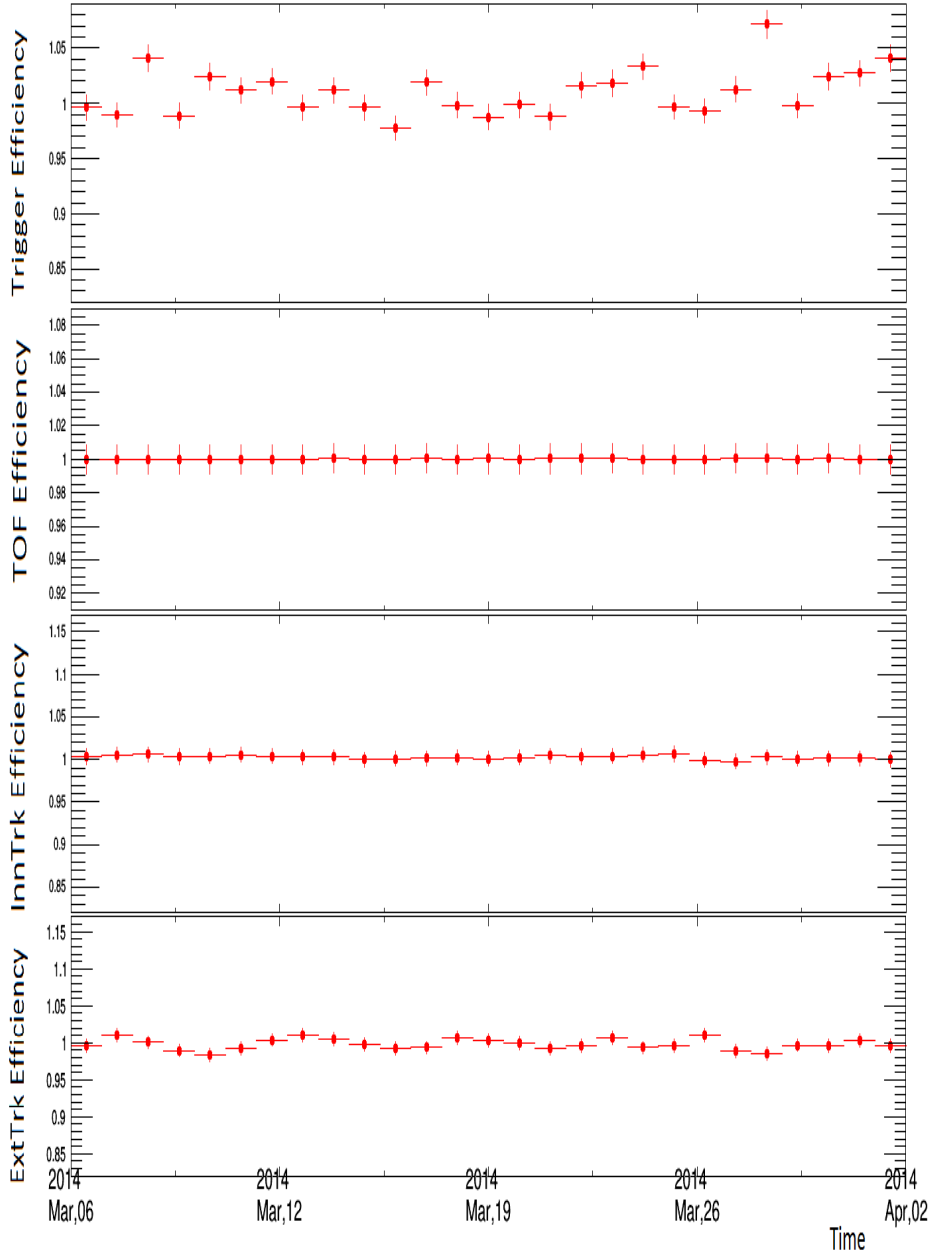
Figure 5.2: The data(t)/data efficiency for the trigger and each of the selected sub-detectors used for the proton flux measurement. From top to bottom these panels represent the trigger, the TOF, the Inner and the External Tracker efficiency for 38th Bartels rotation and for the rigidity bin 4.88-5.37 GV. This analysis is repeated for 69 Bartels rotations and for each rigidity bin to retrieve time dependent proton flux measurement.

64
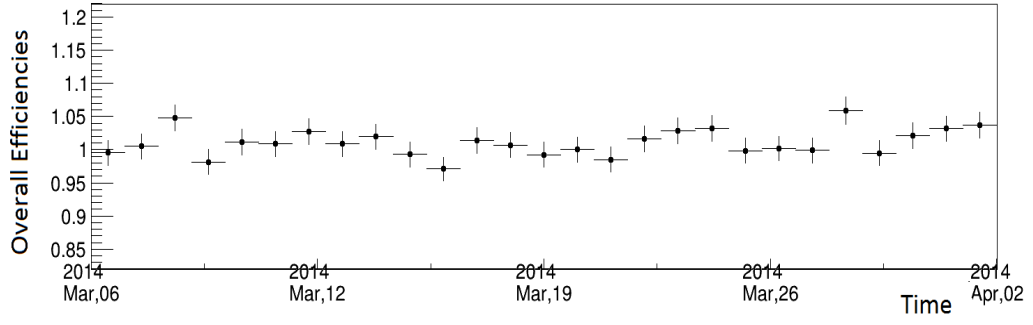
Figure 5.3: The overall time dependent effective efficiency for the proton flux measurement. Time dependent effective efficiency ratio calculation is performed for rigidity bin 4.88-5.37 GV and 38th Bartels rotation between 6 March and 2 April 2014.

5.2 The Unfolded Time Dependent Proton Flux Measurement

The time dependent proton flux measurement is given in Figure 5.4. Events rigidities were corrected using an unfolding method that was described in detail in Chapter 4. Systematic errors are caused by uncertainties in the acceptance, the event selection, the geomagnetic cutoff factor, the rigidity resolution and the unfolding.

The measurement includes 69 Bartels rotations, each of which corresponds to 27 days. Also it was performed for GV-TV rigidity scale and the color axis gives the proton flux in unit of m^{-2} sr^{-1} s^{-1} GV^{-1}. Especially below 30 GV, the proton flux depends on the geomagnetic environment of the Earth and is modulated as a function of time .

A three dimension proton flux measurement versus rigidity in the time interval from July in 2011 to June in 2016 is given in Figure 5.5 . In order to see the detailed behaviour of the proton flux at low rigidities, the rigidity scale is limited to 10 GV. The proton spectra exhibits a large variation with time at low rigidities as expected due to solar activities. At the begin and end of analysis time, flux reaches its maximum values. The solar maximum is observed in April 2014. The proton flux takes minimum value at solar maximum.

65
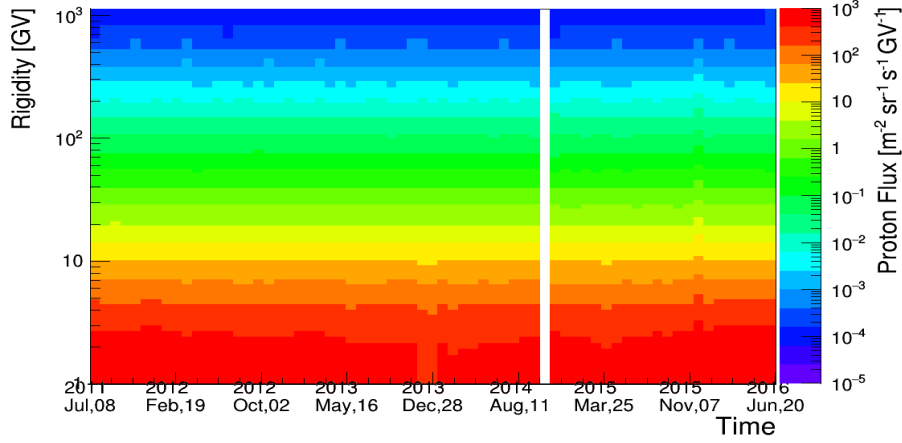
Figure 5.4: The proton flux measurement versus rigidity and time. Time is binned in 69 Bartels rotations starting from 08 July 2011 to 20 June 2016. The x-axis gives operation time of the AMS-02, y-axis gives the measured rigidity and the color scale gives the proton flux. Below 30 GV modulation effects can be observed for some Bartels rotations.
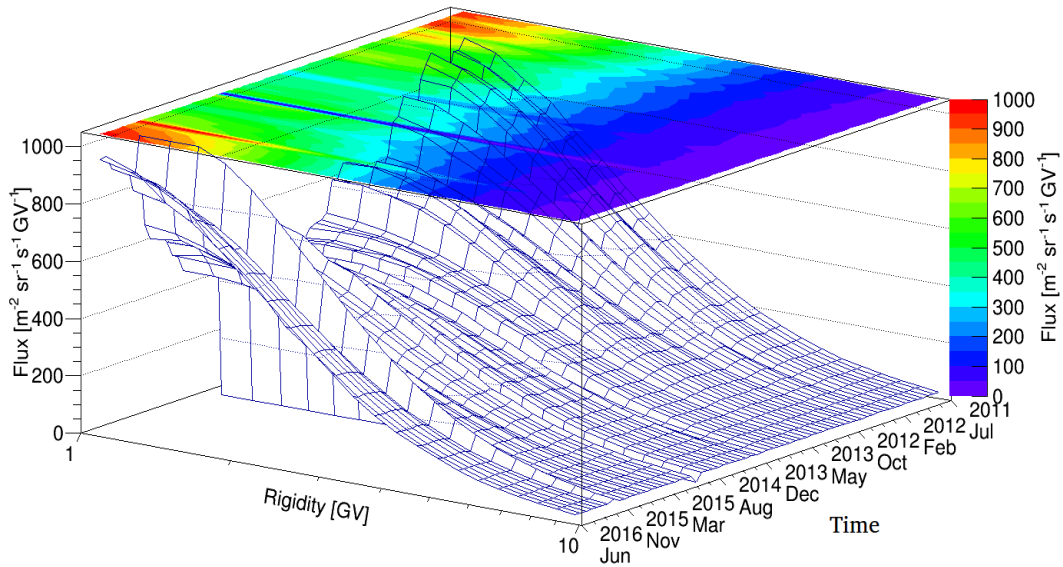
Figure 5.5: The proton flux versus rigidity and time from 08 July 2011 to 20 June 2016. The rigidity scale has been limited to 10 GV to see detailed behaviour of variability of low rigidities of proton flux measurement. At some values proton flux shows no flux because there is no data during the AMS-02 TTCS shut down.

66

The Figure 5.6 shows the proton flux measurements for 1-1.16, 1.16-1.33, 1.51-1.71 GV rigidity intervals for 69 Bartels rotations. The Figure 5.7 shows 2.15-2.40, 2.40-2.67, 3.29-3.64 GV rigidity intervals. Finally the Figure 5.8 shows 5.37-5.90, 10.10-11.00, 21.10-22.80 GV rigidity intervals. In addition, for each figure the bottom-most panel gives the number of sunspots from "Sunspot Index and Long-term Solar Observations" [84] for each time bin. The solar maximum is observed in April 2014. It is clearly can be seen in the first analysis, flux takes a minimum value at the solar maximum. As detailed in Chapter 2, at solar maximum large amounts of material ejected by the Sun carry also a large magnetic disturbance. As a result galactic cosmic rays are affected and some of them are swept away and the flux takes its minimum value at low rigidities at near Earth orbit. Particles with high rigidities can penetrate this magnetic disturbance. Therefore when particle rigidities are getting higher, shown in the second and third figure, the effects of the materials ejected by the Sun are getting lower as well.

Figure 5.6: The proton flux measurements for 3 characteristic bins which are 1-1.16, 1.16-1.33, 1.51-1.71 GV rigidity intervals for 69 Bartels rotations. In addition, the bottom-most panel gives the number of sunspots for each time bin. The comparison of proton flux measurement and the sunspot numbers shows the anti-correlation especially during at solar maximum observed in April 2014.
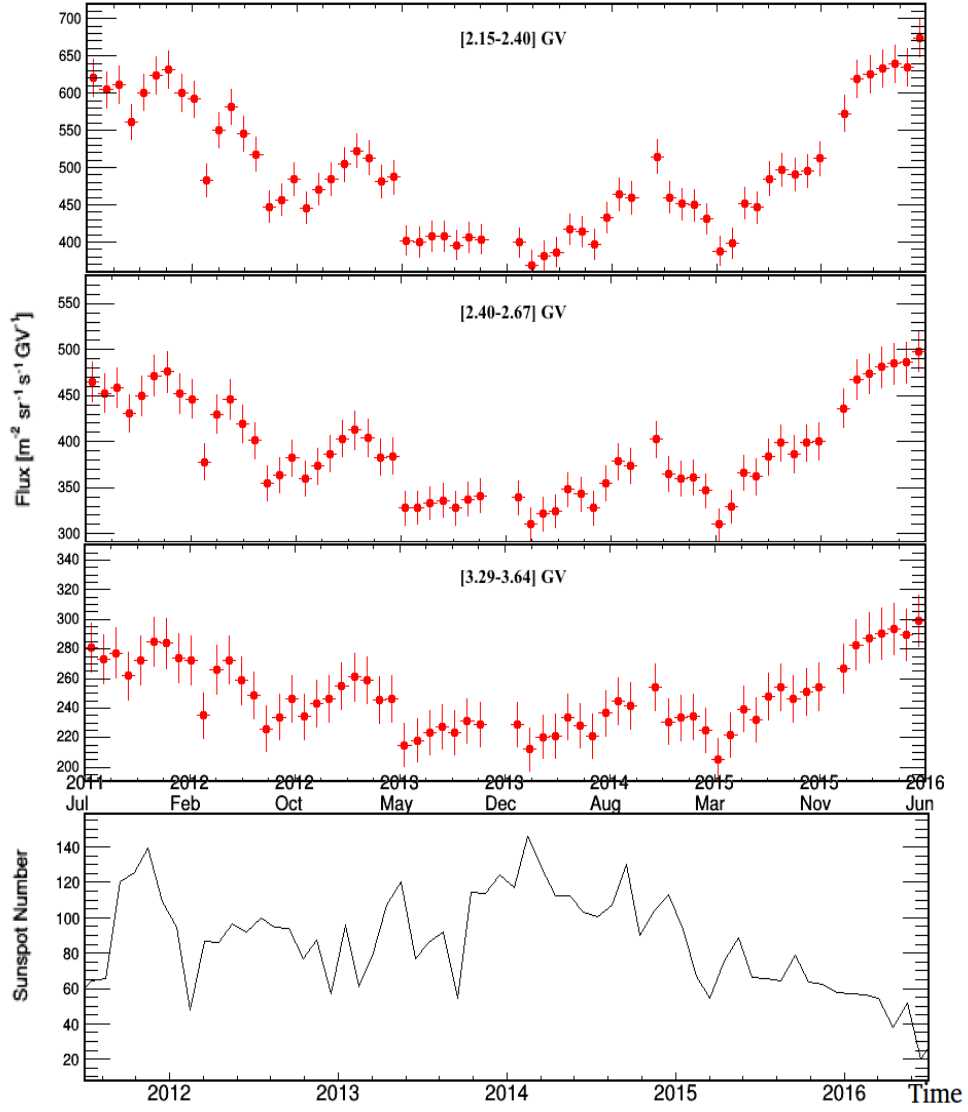
Figure 5.7: Proton flux measurements for 3 characteristic bins which are 2.15-2.40, 2.40-2.67, 3.29-3.64 GV rigidity intervals for 69 Bartels rotations. In addition, the bottom-most panel gives the number of sunspots for each time bin. The comparison of proton flux measurement and the sunspot numbers shows a fore-mentioned decrease especially during at solar maximum observed in April 2014.
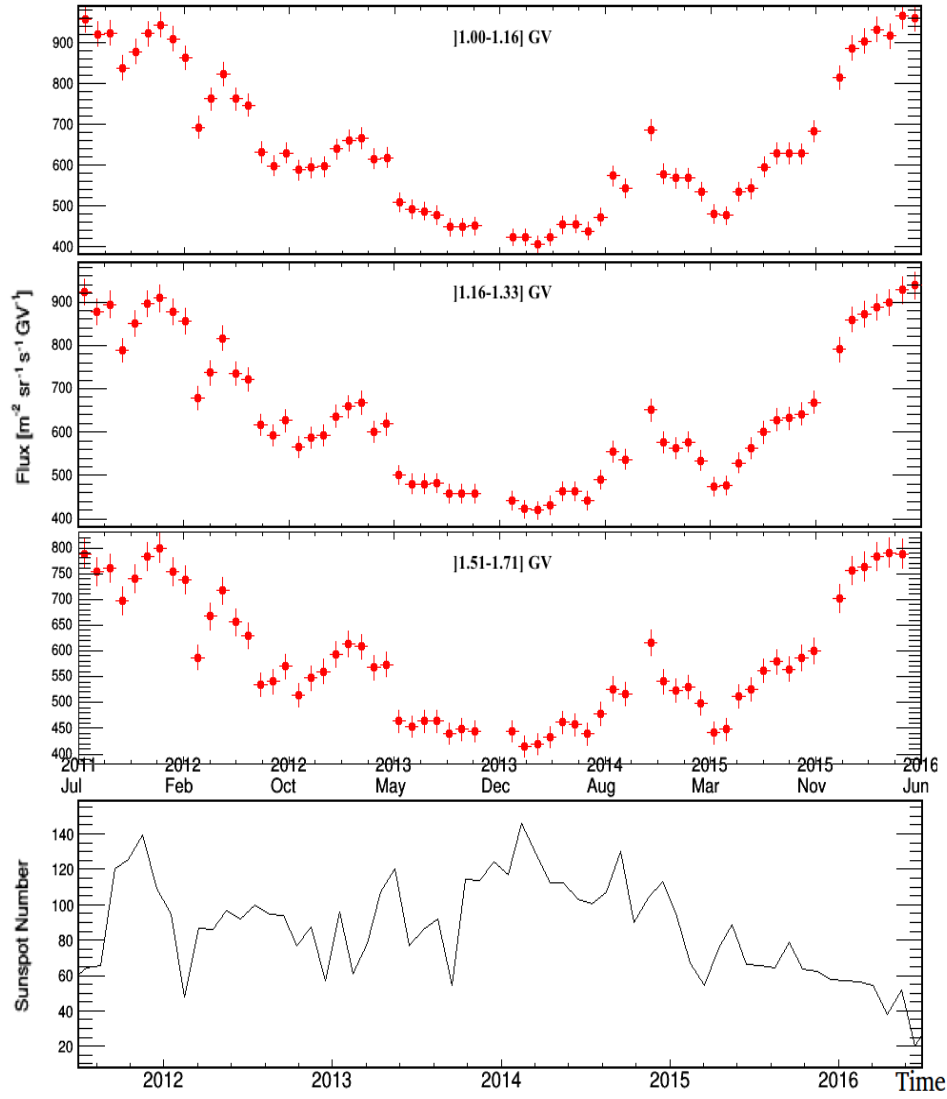
69
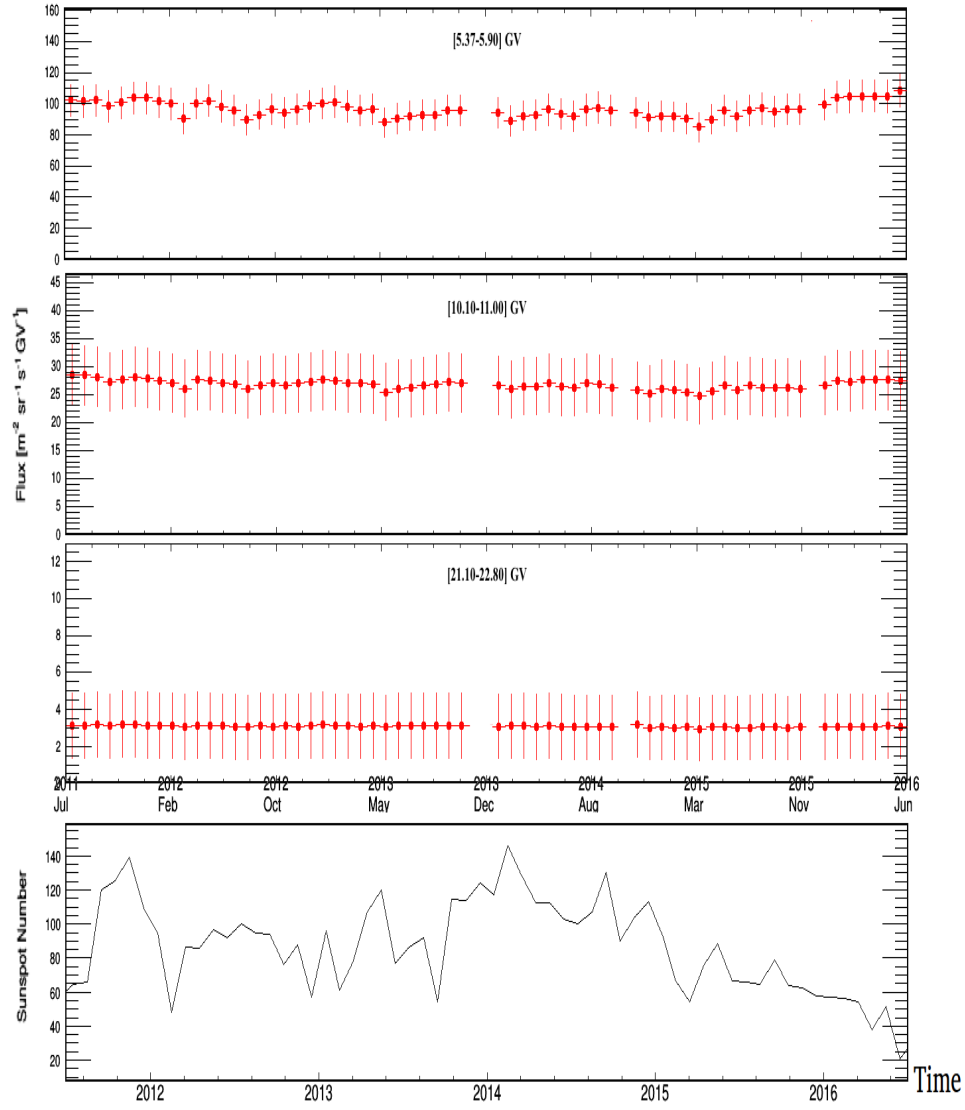
Figure 5.8: Proton flux measurements for 3 characteristic bins which are 5.37-5.90, 10.10-11.00, 21.10-22.80 GV rigidity intervals for 69 Bartels rotations. In addition, the bottom-most panel gives the number of sunspots for each time bin. Comparing to previous analyses, the proton flux has less modulation effect as expected.

70

As detailed in Chapter 2, the Sun has huge energy releases in the form of solar flares and coronal mass ejections. These solar activities change proton flux in near Earth orbit especially during solar maximum. The 11-year solar cycle caused by the 22-year magnetic polarity flip of the Sun was analyzed at low rigidities. Up to 5 GV the proton flux measurements have big deviations which sign solar effects carrying cosmic particles and accompanying magnetic field. These effects are observed in the proton flux measurements performed with AMS-02 data in the concept of Chapter 5. The proton flux takes its minimum value up to ~ 5 GV at the solar maximum observed in April 2014. As proton rigidities are getting higher solar activities effects reach decrease in time.

CHAPTER 6

CONCLUSIONS

AMS-02 is a multipurpose, state-of-the-art, cosmic ray detector which measures CRs with uprecedented statistics and precision on board the International Space Station.

Proton flux measurement provides crucial information regarding origin, acceleration and propagation of cosmic rays. Solar activities can modulate proton flux at low rigidities. The time dependence is related with sunspot numbers which occur on the surface of the Sun. The sunspot numbers reach maximum and minimum during 11-year so called 11-year-solar cycle caused by the 22 year magnetic polarity cycle.

To this end, a full measurement of proton flux is given in the range from 1 GV to 1.8 TV with 5 years of AMS-02 data. A careful selection of proton events was performed through a series of selection regarding the subdetectors determined for the analysis. Each related variable defined in the proton flux formula was analyzed for both AMS-02 data and MC simulation if necessary. Finally, integrated flux for 5 years AMS-02 data was obtained and compared with the AMS-02 published proton flux measurement for both before and after unfolding procedure in order to take resolution effects into account. The comparison given as ratio is inside the total quadratic and systematic errors derived from published measurement. Another comparison between the proton flux measurements performed with the AMS-02 data and SPENVIS predictions up to 100 GeV shows similarity as a function of kinetic energy. The difference comes from the worst-case scenario of the Sun which is taken into account by the SPENVIS.

The proton spectra is observed at low rigidities in order to see recurrent activities of the Sun. The analysis is based on 5.6×10^8 proton events collected in 5 years of oper-

ation. The low rigidity behaviour can be observed not only for several characteristic bins but also three dimensional flux analysis versus rigidity and time. The released energy from the Sun in the form of solar flares and coronal mass ejections affects the geomagnetic environment of the Earth. The solar modulation study includes comparison of sunspot amplitudes with different rigidity bins in order to analyze solar maximum and proton flux correlation.

In conclusion, up to now the proton flux measurements show rigidity dependence as expected in the theoretical conclusions including origin, propagation and acceleration of cosmic rays. However as rigidities are getting higher above TV rigidity spectra, the new results might sign new sources for protons. Moreover, the time modulation of protons shows importance of the Sun at low rigidities. Even though the Sun has very complicated magnetic structure, the solar activities formed by the Sun are repeated in the concept of the 11-year solar cycle caused by the magnetic polarity flip. These results might be used to see how solar activities change Earth's environment for space operations. The methodology including unfolding procedure used in the both time-dependent and time-independent proton flux measurements is a background for other cosmic ray particles measurements. With data recorded by the AMS-02, the new result might sign new sources and show different rigidity dependence in the Galaxy and different modulation dependence of the Sun at low Earth Orbit.

REFERENCES

[1] NASA, "Explainer: the International Space Station," 2013.

[2] M. S. Longair, *High Energy Astrophysics, 3rd edn., by Malcolm S. Longair.* Cambridge University Press, 2011.

[3] M. Paniccia, *Search for Time-dependent Fluctuations in Cosmic Ray Flux with the AMS-01 Detector and Construction of the AMS-02 Detector.* PhD thesis, Geneva University, 2008.

[4] A. A. Pacini, "Cosmic Rays: Bringing Messages From the Sky to the Earth's Surface," *Rev. Bras. Ensino Fís.*, vol. 39, no. 1, pp. 1–10, 2016.

[5] A. D. Santis et al., "Geomagnetic South Atlantic Anomaly And Global Sea Level Rise: A direct connection?," *J. Atmos. Sol. Terr. Phys.*, vol. 74, pp. 129–135, 2012.

[6] P. Picozza et al., "PAMELA - A Payload for Antimatter Matter Exploration and Light-nuclei Astrophysics," *Astropart. Phys.*, pp. 42–47, 2006.

[7] M. Heil, *Measurement of the Positron Fraction in Cosmic Rays from 0.5-350 GeV with the AMS-02 Detector on the International Space Station.* PhD thesis, Karlsruhe Institute of Technology, 2013.

[8] J. Olzem *Nucl. Instrum. Methods Phys. Res., Sect. A*, pp. 285–288, 2005.

[9] S. Ahlen et al., "An antimatter spectrometer in space," *Nucl. Instrum. Methods Phys. Res.*, vol. 350, pp. 351–367, 09 1994.

[10] M. Malberti, "Operation and performance of the CMS tracker," *Proceedings of Science*, vol. 0, no. September 2014, 2014.

[11] C. Turkoglu, *Calorimetric Mode Photon Analysis Using the Alpha Magnetic Spectrometer (AMS-02).* PhD thesis, Middle East Technical University, 2015.

[12] M. Aguilar-Benitez et al., "In-beam aerogel light yield characterization for the AMS RICH detector," *Nucl. Instrum. Methods Phys. Res., Sect. A*, vol. 614, no. 2, pp. 237–249, 2010.

[13] J. Es et al., "AMS02 Tracker Thermal Control System Overview And Spin-Off For Future SpaceCraft Cooling System Developments," *60th International Astronautical Congress 2009, IAC 2009*, 2009.

[14] S. Schael et al., "Precision Measurements of the Electron Spectrum and the Positron Spectrum with AMS," *Icrc2013*, pp. 2–5, 2013.

[15] D. F. Smart and M. A. Shea, "A review of geomagnetic cutoff rigidities for earth-orbiting spacecraft," *Advances in Space Research*, vol. 36, no. 10, pp. 2012–2020, 2005.

[16] M. Aguilar et al., "Precision Measurement of the Proton Flux in Primary Cosmic Rays from 1 GV to 1.8 TV with the Alpha Magnetic Spectrometer on the International Space Station," *Phys. Rev. Lett.*, vol. 114, p. 171103, 2015.

[17] M. Aguilar et al., "First result from the alpha magnetic spectrometer on the international space station: Precision measurement of the positron fraction in primary cosmic rays of 0.5-350 gev," *Phys. Rev. Lett.*, vol. 110, p. 141102, 2013.

[18] M. Aguilar et al., "High statistics measurement of the positron fraction in primary cosmic rays of 0.5-500 GeV with the alpha magnetic spectrometer on the international space station," *Phys. Rev. Lett.*, vol. 113, no. 12, 2014.

[19] M. Aguilar et al., "Precision measurement of the (e++e-) flux in primary cosmic rays from 0.5 GeV to 1 TeV with the alpha magnetic spectrometer on the international space station," *Phys. Rev. Lett.*, vol. 113, no. 22, pp. 1–7, 2014.

[20] M. Aguilar et al., "Electron and positron fluxes in primary cosmic rays measured with the alpha magnetic spectrometer on the international space station," *Proceedings of Science*, vol. 22-29-July, no. September, pp. 1–9, 2015.

[21] M. Aguilar et al., "Precision Measurement of the Helium Flux in Primary Cosmic Rays of Rigidities 1.9 GV to 3 TV with the Alpha Magnetic Spectrometer on the International Space Station," *Phys. Rev. Lett.*, vol. 115, no. 21, 2015.

[22] M. Aguilar et al., "Antiproton Flux, Antiproton-to-Proton Flux Ratio, and Properties of Elementary Particle Fluxes in Primary Cosmic Rays Measured with the Alpha Magnetic Spectrometer on the International Space Station," *Phys. Rev. Lett.*, vol. 117, no. 9, 2016.

[23] M. Aguilar et al., "Precision Measurement of the Boron to Carbon Flux Ratio in Cosmic Rays from 1.9 GV to 2.6 TV with the Alpha Magnetic Spectrometer on the International Space Station," *Phys. Rev. Lett.*, vol. 117, no. 23, 2016.

[24] M. Aguilar et al., "Observation of the Identical Rigidity Dependence of He, C, and O Cosmic Rays at High Rigidities by the Alpha Magnetic Spectrometer on the International Space Station," *Phys. Rev. Lett.*, vol. 251101, no. December, pp. 1–8, 2017.

[25] M. Aguilar et al., "Observation of New Properties of Secondary Cosmic Rays Lithium, Beryllium, and Boron by the Alpha Magnetic Spectrometer on the International Space Station," *Phys. Rev. Lett.*, vol. 120, no. 2, p. 021101, 2018.

[26] M. Aguilar et al., "Observation of Complex Time Structures in the Cosmic-Ray Electron and Positron Fluxes with the Alpha Magnetic Spectrometer on the International Space Station.," *Phys. Rev. Lett.*, vol. 121, no. 5, p. 051103, 2018.

[27] M. Aguilar et al., "Precision Measurement of Cosmic-Ray Nitrogen and its Primary and Secondary Components with the Alpha Magnetic Spectrometer on the International Space Station," *Phys. Rev. Lett.*, vol. 121, no. 5, p. 051103, 2018.

[28] M. Aguilar et al., "Observation of Fine Time Structures in the Cosmic Proton and Helium Fluxes with the Alpha Magnetic Spectrometer on the International Space Station," *Phys. Rev. Lett.*, pp. 1–13.

[29] V. F. Hess, "Über Beobachtungen der durchdringenden Strahlung bei sieben Freiballonfahrten," *Phys. Z.*, vol. 13, pp. 1084–1091, 1912.

[30] J. Blümer, R. Engel, and J. R. Hörandel, "Cosmic rays from the knee to the highest energies," *Prog. Part. Nucl. Phys.*, vol. 63, no. 2, pp. 293–338, 2009.

[31] B. Bijay, P. Banik, and A. Bhadra, "The knee in the cosmic ray energy spectrum from the simultaneous EAS charged particles and muon density spectra," *Astrophys. Space Sci.*, vol. 361, no. 9, pp. 1–10, 2016.

[32] A. Haungs, "Cosmic Rays from the Knee to the Ankle," *Physics Procedia*, vol. 61, pp. 425–434, 2015.

[33] G. T. Zatsepin and V. A. Kuz'min, "Upper limit of the spectrum of cosmic rays," *J. Exp. Theor. Phys.*, vol. 4, p. 78, 1966.

[34] V. Vagelli, *Measurement of the Cosmic $e++e-$ Flux from 0.5 GeV to 1 TeV with the Alpha Magnetic Spectrometer (AMS-02) on the International Space Station.* PhD thesis, Karlsruhe Institute of Technology, 2014.

[35] R. Aloisio, V. Berezinsky, and A. Gazizov, "Transition from galactic to extragalactic cosmic rays," *Astropart. Phys.*, vol. 39-40, no. 1, pp. 129–143, 2012.

[36] G. A. Bazilevskaya, "Solar cosmic rays in the near Earth space and the atmosphere," *Adv. Space Res.*, vol. 35, no. 3, pp. 458–464, 2005.

[37] V. Ptuskin, V. Zirakashvili, and E. S. Seo, "Spectra of cosmic-ray protons and helium produced in supernova remnants," *Astrophys. J.*, vol. 763, no. 1, 2013.

[38] V. Berezinsky, "Extragalactic cosmic rays and their signatures," *Astropart. Phys.*, vol. 53, no. C, pp. 120–129, 2014.

[39] W. Baade and F. Zwicky, "Remarks on super-novae and cosmic rays [6]," *Phys. Rev. Lett.*, vol. 46, no. 1, pp. 76–77, 1934.

[40] E. Teller, "The origin of cosmic radiation," *Phys. Today*, vol. 2, no. 8, pp. 6–13, 1949.

[41] D. H. Perkins, *Particle Astrophysics.* Oxford University Press, 2 ed., 2003.

[42] "Extragalactic magnetic fields Retrieved from "https://ned.ipac.caltech.edu/level5/March01/Battaner/node33.html"."

[43] K. Ferrièr, "Interstellar magnetic fields: from Galactic scales to the edge of the heliosphere," *Journal of Physics: Conference Series*, 2015.

[44] A. W. Strong, I. V. Moskalenko, and V. S. Ptuskin, "Cosmic-ray propagation and interactions in the galaxy," *Annu. Rev. Nucl. Part. Sci.*, vol. 57, pp. 285–327, 2007.

[45] E. Herbst, "Chemistry in the Interstellar Medium," *Annu. Rev. Phys. Chem.*, vol. 46, no. 1, pp. 27–54, 1995.

[46] R. Cowsik et al., "Steady State of Cosmic-Ray Nuclei—Their Spectral Shape and Path Length at Low Energies," *Phys. Rev.*, vol. 158, no. 5, pp. 1238–1242, 1967.

[47] A. Balogh and V. Izmodenov, "The Heliosphere and Its Boundaries," *ISSI Scientific Reports Series*, pp. 151–163, 1955.

[48] J. D. Keyser and S. Stankov, "Earth's magnetosphere and ionosphere," *KBVE Review E Tijdschrift - Journal of the Royal Belgian Association of Electrical Engineers (KBVE)*, no. January 2015, 2014.

[49] K. Herbst, A. Kopp, and B. Heber, "Influence of the terrestrial magnetic field geometry on the cutoff rigidity of cosmic ray particles," *Ann. Geophys.*, vol. 31, no. 10, pp. 1637–1643, 2013.

[50] M. S. Potgieter, "Solar modulation of cosmic rays," *Living Reviews in Solar Physics*, vol. 10, 2013.

[51] D. H. Hathaway, "The Solar Cycle," *Living Rev. Sol. Phys.*, pp. 1–81, 2015.

[52] I. Sandberg et al., "Solar flares, coronal mass ejections and solar energetic particle event characteristics," *J. Space Weather Space Clim.*, vol. 6, p. A42, 2016.

[53] K. Cantner, "Here comes the solar maximum: What we know - and don't know - about solar storms and their hazards," 2012.

[54] J. Bartels, "Twenty-seven day recurrences in terrestrial-magnetic and solar activity, 1923–1933," *J. Geophys. Res.*.

[55] A. Belov et al., "What determines the magnitude of forbush decreases?," *Adv. Space Res.*, vol. 27, no. 3, pp. 625–630, 2001.

[56] E. Flückiger et al., "The cosmic ray ground level enhancement during the Forbush decrease in January 2005," *... Cosmic Ray ...*, no. January, pp. 225–228, 2005.

[57] D. V. Reames and C. K. Ng, "Heavy-Element Abundances in Solar Energetic Particle Events," *Astrophys. J.*, vol. 610, pp. 510–522, 2004.

[58] D. J. Griffiths, "David Jeffery Griffiths-Introduction to Elementary Particles, 2nd Edition-Wiley-VCH (2008)."

[59] J. W. F. Valle and J. Schechter, "Neutrino masses in SU(2) x U(1) theories," *Phys. Rev. D: Part. Fields*, vol. 22, no. 9, pp. 2227–2235, 1980.

[60] B. Dolgoshein, "Transition radiation detectors," *Nucl. Instrum. Methods Phys. Res., Sect. A*, vol. 326, pp. 434–469, 1993.

[61] U. J. Becker, T. Supervisor, and T. Greytak, *A Transition Radiation Detector and Gas Supply System for AMS Bilge Melahat Demirköz.* PhD thesis, Massachusetts Institute of Technology, 2004.

[62] M. Behlmann, *Measurement of Helium Isotopic Composition in Cosmic Rays with AMS-02.* PhD thesis, Massachusetts Institute of Technology, 2018.

[63] L. Yang, *Measurement of the Carbon and Oxygen Fluxes and their Ratio in Cosmic Rays with the AMS Experiment on the International Space Station THÈSE.* PhD thesis, Geneva University, 2017.

[64] K. Lübelsmeyer et al., "Upgrade of the Alpha Magnetic Spectrometer (AMS-02) for long term operation on the International Space Station (ISS)," *Nucl. Instrum. Methods Phys. Res., Sect. A*, vol. 654, no. 1, pp. 639–648, 2011.

[65] J. Alcaraz et al., "The alpha magnetic spectrometer silicon tracker: Performance results with protons and helium nuclei," *Nucl. Instrum. Methods Phys. Res., Sect. A*, vol. 593, no. 3, pp. 376–398, 2008.

[66] M. Tanabashi et al., "27. Passage of Particles Through Matter," *Dbcompas.Ihep.Su*, vol. 1, no. April 2006, pp. 1–34, 2007.

[67] G. Alberti et al., "Development of a Thermal Control System with Mechanically Pumped CO2 Two-Phase Loops for the AMS-02 Tracker on the ISS," *arXiv preprint arXiv:1302.4294*, 02 2013.

[68] V. Bindi et al., "The scintillator detector for the fast trigger and time-of-flight (TOF) measurement of the space experiment AMS-02," *Nucl. Instrum. Methods Phys. Res., Sect. A*, vol. 623, no. 3, pp. 968–981, 2010.

[69] A. Battiston, R. and Oliva, "AMS-02 webpage."

[70] V. Bindi et al., "The time of flight detector of the AMS-02 experiment on the international space station," *Nucl. Instrum. Methods Phys. Res., Sect. A*, vol. 718, pp. 478–480, 2013.

[71] V. Bindi et al., "Calibration and performance of the AMS-02 time of flight detector in space," *Nucl. Instrum. Methods Phys. Res., Sect. A*, vol. 743, pp. 22–29, 2014.

[72] S. Schael et al., "The AMS-02 Anticoincidence Counter," *Nucl. Phys. B*, vol. 197, no. 1, pp. 15–18, 2009.

[73] F. Giovacchini, "Performance in space of the AMS-02 RICH detector," *Nucl. Instrum. Methods Phys. Res., Sect. A*, vol. 766, pp. 57–60, 2014.

[74] M. Graziani, "Electron/proton separation and analysis techniques used in the AMS-02 (e++e-) flux measurement," *Nuclear and Particle Physics Proceedings*, vol. 273-275, pp. 2351–2353, 2016.

[75] M. Vecchi et al., "The electromagnetic calorimeter of the AMS-02 experiment," *Nucl. Phys. B Proc. Suppl.*, 2012.

[76] G. Ambrosi et al., "In-flight operations and status of the AMS-02 silicon tracker," *Proceedings of Science*, vol. 30-July-20, pp. 1–7, 2015.

[77] A. Kounine and V. Koutsenko, "Flight Software for xDR and JINx nodes in AMS-02," *Event (London)*, no. October, pp. 1–52, 2008.

[78] C. Finlay et al., "International Geomagnetic Reference Field: The eleventh generation," *Geophys. J. Int.*, vol. 183, no. 3, pp. 1216–1230, 2010.

[79] J. Alcaraz et al., "Leptons in near earth orbit," *Phys. Lett. B*, no. June, pp. 10–22, 2000.

[80] J. D. Sullivan, "Geometric factor and directional response of single and multi-element particle telescopes," *Nucl. Instrum. Methods*, vol. 95, no. 1, pp. 5–11, 1971.

[81] G. D'Agostini, "A multidimensional unfolding method based on Bayes' theorem," *Nucl. Instrum. Methods Phys. Res., Sect. A*, vol. 362, no. 2-3, pp. 487–498, 1995.

[82] The MAGIC Collaboration and J. Albert, "Unfolding of differential energy spectra in the MAGIC experiment," *Nucl. Instrum. Methods Phys. Res., Sect. A*, no. February, pp. 1–28, 2007.

[83] CALTECH, "Bartels Rotation Numbers and Dates for Years 2004 - 2023," tech. rep.

[84] ICSU-WDS, "Sunspot Index and Long-term Solar Observations," tech. rep., World Data Center, 2017.